DEPARTMENT OF PHYSICS, UNIVERSITY OF JYVÄSKYLÄ

IDENTIFIED CHARGED PARTICLE FLOW AND UNFOLDING EVENT-BY-EVENT FLOW IN HEAVY ION COLLISIONS

BY
TOMAS SNELLMAN

Master's thesis

Supervisors: Jan Rak, Dong Jo Kim

Jyväskylä, Finland
December, 2013

Abstract

In this thesis I study two aspects related to anisotropic flow coefficients v_2 and v_3 in heavy-ion collisions. The study is done for Pb-Pb collisions at $\sqrt{s_{NN}} = 2.76$ TeV using data simulated by A MultiPhase Transport (AMPT) model. First I study flow of identified charged particles, pions, kaons and protons. At RHIC in Au-Au collisions at $\sqrt{s_{NN}} = 200$ GeV it has been observed that scaling v_2 of identified hadrons with the number of quarks and plotting it as a function of transverse kinetic energy KE_T produces almost perfect scaling between different particle species. This was taken as an indication that flow is mainly generated in the partonic phase and is not strongly affected by the hadronic phase. However, in Pb-Pb collisions at $\sqrt{s_{NN}} = 2.76$ TeV in LHC the scaling has been observed to break down. AMPT model uses a simple quark coalescence model, which was used to explain the scaling at RHIC energies. Because of the scaling breakdown at LHC the coalescence model has been challenged in the field. In my studies I have observed that AMPT does not produce perfect quark number scaling, even though it would be expected because of the coalescence model.

Another aspect studied here is event-by-event flow. Event-by-event flow is connected to the fluctuations in the initial collisions. Only recently the field has started to study fluctuations and event-by-event flow. I will show distributions of event-by-event flow coefficients in the AMPT model. In addition to the true fluctuations the distributions have a significant smearing component from limited resolution resulting from finite multiplicity in a single event. I will use a data-driven unfolding method based on an iterative Bayesian procedure to remove the smearing effects. I will test the procedure in a toy Monte Carlo simulation to test its performance and apply it to AMPT data. I have observed that based on the Monte Carlo the procedure works for v_2 in general and for v_3 in central collisions.

Contents

List of Figures

1 Introduction

At sufficiently high energies quarks and gluons are no longer bound to hadrons, but they form a deconfined state known as Quark-Gluon plasma (QGP). The main goal of heavy-ion physics is the study of QGP and its properties. One of the experimental observables that is sensitive to the properties of QGP is the azimuthal distribution of particles in the plane perpendicular to the beam direction.

When nuclei collide at non-zero impact parameter (non-central collisions), the geometrical overlap region is asymmetric. This initial spatial asymmetry is converted via multiple collisions into an anisotropic momentum distribution of the produced particles. For low momentum particles ($p_{\mathrm{T}} \lesssim 3$ GeV/c), this anisotropy is understood to result from hydrodynamically driven flow of the QGP [1–5].

One way to characterize this anisotropy is with coefficients from a Fourier series parametrization of the azimuthal angle distribution of emitted hadrons. The second order coefficient, which is also known as elliptic flow, shows clear dependence on centrality. The collision geometry is mainly responsible for the elliptic flow. Higher harmonics don't depend that much on centrality. These higher harmonics carry information about the fluctuations in collisions. The event-by-event fluctuations have an increasing importance in measurements.

In this master's thesis identified charged particle flow and quark number scaling is studied at LHC energies in A MultiPhase Transport (AMPT) [6, 7] model. AMPT is a hybrid transport model, which models an ultra-relativistic nuclear collision using many tools of Monte Carlo simulation. The results are compared to ALICE results. In my Bachelor's thesis I studied methods to determine the event plane and flow coefficients in heavy-ion collisions with AMPT data. In this thesis I have performed further analysis on the AMPT data and studied flow coefficients of identified charged particles.

One important aspect in flow of different particle species has been quark number scaling. At RHIC energies $\sqrt{s_{NN}} = 200$ GeV it was found to work almost perfectly for pions, kaons and protons. This was taken as a strong indication that anisotropic flow at RHIC develops primarily in the partonic phase, and is not strongly influenced by the subsequent hadronic phase [8]. At LHC in Pb-Pb collisions $\sqrt{s_{NN}} = 2.76$ TeV it was observed that for proton v_2 the quark number scaling does not work [8]. The RHIC observations were explained by assuming that hadronization occurs through a simple quark coalescence model, where three nearest quarks are combined into a hadron or nearest quark-antiquark pair forms a meson. AMPT model, that I study, uses this quark coalescence model and therefore it is important to see whether it produces quark number scaling.

Another aspect that I studied is event-by-event flow and the unfolding method. Unfolding is used to restore the original v_n distribution from the observed distribution, that is significantly smeared by limited resolution resulting from finite

multiplicity in a single event. In this thesis I use a data-driven unfolding method based on an iterative Bayesian procedure. I first test the performance in a toy Monte Carlo simulation and later apply it to the AMPT data. Knowing the performance of unfolding is required to know how reliable measured event-by-event distributions are.

For future studies also the correlation between observed and true v_n is important. It has been proposed that studying jet properties separately for events with strong or weak anisotropy would shed some new light on path length dependence and energy loss models. For the separation on an event-by-event basis one has to keep in mind the relation between observed and true v_n.

This thesis is organised as follows: In the first section I will discuss Quantum Chromodynamics, its history, its properties and how it leads to quark-gluon plasma. I will give a brief introduction to the motivation and history of heavy-ion physics. At the end of this chapter I will give an example of how study of heavy-ion physics is related to string theory and the search for physics beyond the standard model.

In section 2 I discuss the features of heavy-ion collisions. I present basic physics behind the studied phenomena in more detail. I will discuss flow, its origins, its relation to energy loss models and the two phenomena studied in this thesis, fluctuating events and identified charged particle flow. I present results from RHIC and LHC measurements of identified particle flow. Here I also define quark number scaling and the quark coalescence model used to explain it.

In section 3 I present the methods I use in this thesis to study anisotropic flow. I will show the event plane method used to calculate flow coefficients and the two sub event method used to estimate event plane resolutions. Also in this section I will present the unfolding procedure and a simple Monte Carlo simulation testing the performance of this procedure.

In section 4 I introduce the AMPT model used to generate the data I study in this thesis. I will go through the components used in the model. This is followed by my analysis in section 5. I will show my analysis and my results on identified particle flow and unfolding event-by-event distributions.

Finally I will discuss my results in section 6 and summarize my thesis in 7.

1.1 Quantum chromodynamics

1.1.1 Foundation of QCD

There are four known basic interactions in the universe: gravity, electromagnetic, weak and strong interactions. The standard model of particle physics includes three of these excluding the gravitational interaction. The theory of strong interactions is known as Quantum Chromodynamics (QCD).

The development of QCD began after the introduction of new powerful particle accelerators that were capable of particle physics research in the 1950s. Before this particles were mainly discovered from cosmic rays. Positrons, neutrons and muons were discovered in the 1930s and charged pions were discovered in 1947 [9]. The neutral pion was discovered in 1950 [10].

The Lawrence Berkeley National Laboratory started the Bevalac accelerator in 1954, Super Proton Synchrotron (SPS) in CERN began operating in 1959 and the Alternating Gradient Synchrotron at Brookhaven started in 1960. With an energy of 33 GeV AGS was the most powerful accelerator of that time. By the beginning of 1960s several new particles had been discovered. These include antiprotons, antineutrons, Δ-particles and the six hyperons (Ξ^0, Ξ^-, $\Sigma^\pm$, Σ^0 and Λ).

Facing this number of different particles started the search for symmetries. Already in 1932 Heisenberg [11] had proposed an isospin model to explain similarities between the proton and the neutron. In 1962 Gell-Mann and Ne'eman presented that particles sharing the same quantum numbers (spin, parity) could be organised using the symmetry of SU(3). [12] Heisenberg's Isospin model followed the symmetry of SU(2). Using the SU(3) model known baryons and mesons could be presented as octets. This also lead to the discovery of the Ω^- particle since this was missing from the SU(3) decuplet that included heavier baryons.

The most simple representation of SU(3) is a triplet. Inside this triplet particles would have electric charges $2/3$ or $-1/3$. However, these had not been detected. In 1964 Gell-Mann [13] and Zweig proposed that baryons and mesons would be bound states of these three hypothetical triplet particles that Gell-Mann called quarks. Now we know that these are the u, d and s quarks. The original quark model had still problems; it was violating the Pauli exclusion principle. For example the Ω^- particle is comprised of three s quarks, two of which would have exactly the same quantum states.

The problem was solved by the colour quantum number. The first to present the idea of colour had been Greenberg already in 1964 [14]. In 1971 Gell-Mann and Frtizsch presented their model, which solved the antisymmetry problem. They added a colour quantum number to quarks, which separated quarks of the same species. In the new colour model the baryonic wave function became

$$(qqq) \to (q_r q_g q_b - q_g q_r q_b + q_b q_r q_g - q_r q_b q_g + q_g q_b q_r - q_b q_g q_r)\,, \tag{1}$$

The colour model was also supported by experimental evidence. The decay rate of a neutral pion with the addition of colours is

$$\Lambda\left(\pi^0 \to \gamma\gamma\right) = \frac{\alpha^2}{2\pi}\frac{N_c^2}{3^2}\frac{m_\pi^3}{f_\pi^2}. \tag{2}$$

For $N_c = 3$ this gives 7.75 eV and the measured value is (7.86 ± 0.54) eV [15].

Another observable that combines the colour information to the number of quark flavours is The Drell-Ratio R [16]

$$R = \frac{\sigma\left(e^+ + e^- \to \text{hadrons}\right)}{\sigma\left(e^+ + e^- \to \mu^+ + \mu^-\right)} = N_c \sum_f Q_f^2 \tag{3}$$

This has the numerical value 2 when including the three light quarks u, d and s. When the collision energy reaches the threshold of heavy quark (c and b) production processes this increases to 10/3 (for $f = u, d, s, c$) and 11/3 (for $f = u, d, s, c, b$). The threshold of $t\bar{t}$ production, $\sqrt{s} \approx 350$ GeV has not been reached so far by any e^+e^- colliders.

The colour model explained why no free quarks had been observed. Only colour neutral states are possible. The simplest ways of producing a colour neutral object are the combination of three quarks, and the combination of a quark-antiquark pair. These are known as baryons and mesons.

After the addition of colour the main ingredients of QCD had been established. The final quantum field theory of Quantum Chromodynamics formed quickly between 1972 and 1974. Main part of this was the work Gross, Wilczek, Politzer and George did for non-abelian gauge field theories [17–21]. Gross, Wilczek and Politzer received the Nobel Prize in Physics for their work in 2004.

The role of gluons was as a colour octet was presented by Fritzsch, Gell-Mann and Leutwyler in 1973 [22]. The theory had now 8 massless gluons to mediate the strong interaction. Unfortunately these gluons had not been observed experimentally . Indirect evidence of the existence had been seen as it was observed that only about half of the momentum of protons was transported by the quarks [23]. Direct evidence should be seen in electron-electron collisions as a third, gluonic, jet in addition to two quark jets. Three jet events were first seen in 1979 at the PETRA accelerator at DESY [24–26].

1.1.2 Asymptotic Freedom and Deconfinement of Quarks and Gluons

In Quantum Electrodynamics (QED) the electric charge is screened. In the vicinity of a charge, the vacuum becomes polarized. Virtual charged particle-antiparticle pairs around the charge are arranged so that opposing charges face each other. Since the pairs also include an equal amount of opposite charge compared to the original charge the average charge seen by an observer at a distance is smaller. When the distance to the charge increases the effective charge decreases until the coupling constant of QED reaches the fine-structure constant $\alpha = \frac{1}{137}$.

Contrary to QED, QCD is a non-abelian theory. In other words the generators of the symmetry group of QCD, SU(3), do not commute. This has the practical consequence that gluons, that have a colour charge, interact also with other gluons, whereas in QED the electrically neutral carrier particles, photons, only interact with charged particles.

The colour charges in QCD lead to a similar screening effect as in QED, but QCD includes also antiscreening because the gluons can also interact with other gluons. In QCD the antiscreening effect is stronger than screening and in total colour charges are antiscreened. For larger distances to the colour charge the coupling constant is larger. This explains why no free colour charges can be observed. When the distance between charges increases the interaction grows until it is strong enough to produce a new quark-antiquark pair [27].

On the other hand for very small distances the coupling constant approaches 0. This is called asymptotic freedom. For large energies and small distances the coupling constant becomes negligible. In 1975 Collins [28] predicted a state where individual quarks and gluons are no longer confined into bound hadronic states. Instead they form a bulk QCD matter that Shuryak called Quark-Gluon plasma in his 1980 review of QCD and the theory of superdense matter [29].

Though QGP was predicted its properties are still obscure. Even with the final theory of QCD making testable predictions is extremely difficult. The traditional approach in quantum mechanics, perturbation theory, only works when the interaction is weak. In QCD this requires high energy or short distance interactions. Perturbative QCD (pQCD) [30] can be used to calculate processes like the Drell ratio.

Most of the processes can not be calculated directly with pQCD. For example the hadron structure is nonperturbative because of colour confinement. In proton-proton collision experiments one can use the QCD factorisation theorem, where cross-section is separated into two parts: short-distance parton cross section that can be calculated with pQCD and the universal long-distance functions which can be measured with global fits to experiments.

For non-perturbative processes, like the ones present in QGP, one usually turns to Lattice QCD. It is a lattice gauge theory formulated on a discrete Euclidean

space time grid. When the size of the lattice is taken infinitely large and its sites infinitesimally close to each other, the continuum QCD is recovered. Since no new parameters or field variables are introduced in this discretization, LQCD retains the fundamental character of QCD [31].

Lattice QCD has provided the theoretical approximations about the temperature needed for QGP formation. The results from lattice calculation are shown in Fig. 1 [32]. The transition from hadronic matter to QGP is sharp. Thus QGP can be seen as a separate state of matter.

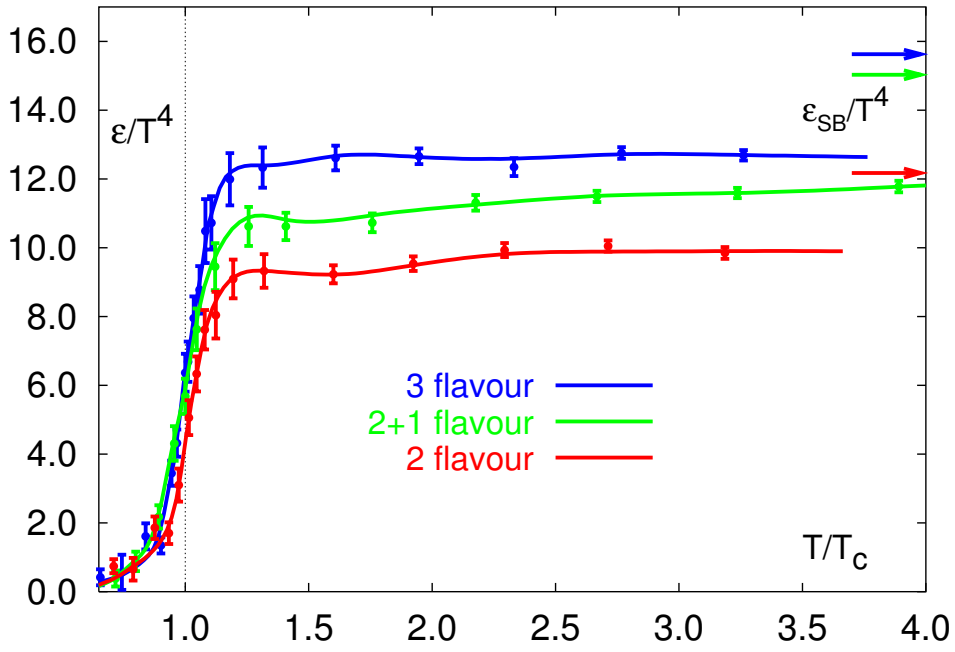

Figure 1: Lattice QCD results [32] for the energy density / T^4 as a function of the temperature scaled by the critical temperature TC. Note the arrows on the right side indicating the values for the Stefan-Boltzmann limit. [1]

A schematic view of a phase diagram for QCD matter as a function of temperature and the baryochemical potential is shown in Fig. 2. The baryochemical potential μ represents the imbalance between quarks and antiquarks. At zero temperature this corresponds to the number of quarks but at higher temperatures there are also additional pairs of quarks and antiquarks. At zero temperature with increasing μ the density is zero up to the onset transition where it jumps to nuclear density, and then rises with increasing μ. Neutron stars are in this region of the phase diagram, although it is not known whether their cores are dense enough to reach the quark matter phase. Along the vertical axis the temperature rises,

taking us through the crossover from a hadronic gas to the quark-gluon plasma. This is the regime explored by high-energy heavy-ion colliders.

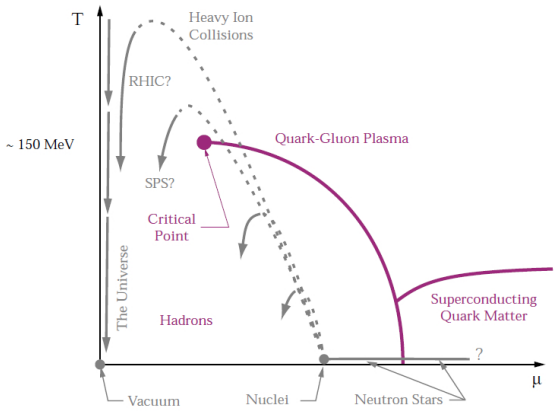

Figure 2: A schematic outline for the phase diagram of QCD matter at ultra-high density and temperature. [33]

Lattice QCD predicts a phase transformation to a quark-gluon plasma at a temperature of approximately $T \approx 170$ MeV $\approx 10^{12}$ K [1]. This transition temperature corresponds to an energy density $\epsilon \approx 1$ GeV/fm^3, nearly an order of magnitude larger than that of normal nuclear matter. Thus producing QGP requires extreme conditions that existed in the early universe at the age of 10^{-6} s after the Big Bang and are nowadays experimentally achievable in heavy-ion collisions. The study of QCD matter at high temperature is of fundamental and broad interest. The phase transition in QCD is the only phase transition in a quantum field theory that can be experimentally probed by any present or foreseeable technology.

1.2 Heavy-Ion physics

The Quark Gluon Plasma (QGP) is experimentally accessible by through collisions of heavy atomic nuclei at ultra-relativistic energies. Its properties and phase transitions between hadronic matter and QGP can be explored through heavy-ion physics. Because of the difficulties in theoretical approaches to QGP heavy-ion physics is a field driven by experimental evidence. Thus the development of heavy-ion physics is strongly connected to the development of particle colliders.

The first heavy-ion collisions were done at the Bevalac experiment at the Lawrence Berkeley National Laboratory [34] and at the Joint Institute for Nuclear Research in Dubna [35] at energies up to 1 GeV per nucleon. In 1986 the Super Proton Synchrotron (SPS) at CERN started to look for QGP signatures in O+Pb collisions. The center-of-mass energy per colliding nucleon pair $\left(\sqrt{s_{NN}}\right)$ was 19.4 GeV [36]. These experiments did not find any decisive evidence of the existence of QGP. In 1994 a heavier lead (Pb) beam was introduced for new experiments at $\sqrt{s_{NN}} \approx 17$ GeV. At the same time the Alternating Gradient Synchrotron (AGS) at BNL, Brookhaven collided ions up to ^{32}S with a fixed target at energies up to 28 GeV [37]. Hints of QGP were already seen at SPS. Although the discovery of a new state of matter was reported at CERN, these experiments provided no conclusive evidence of QGP. Now SPS is used with 400 GeV proton beams for fixed-target experiments, such as the SPS Heavy Ion and Neutrino Experiment (SHINE) [38], which tries to search for the critical point of strongly interacting matter.

The Relativistic Heavy Ion Collider (RHIC) at BNL in New York, USA started its operation in 2000. The top center-of-mass energy per nucleon pair at RHIC, 200 GeV, was reached in the following years. The results from the experiments at RHIC have provided a lot of convincing evidences that QGP was created [1, 2, 39, 40].

The newest addition to the group of accelerators capable of heavy-ion physics is the Large Hadron Collider (LHC) at CERN, Switzerland. LHC started operating in November 2009 with proton-proton collisions. First Pb-Pb heavy-ion runs started in November 2010 with $\sqrt{s_{NN}} = 2.76$ TeV, an energy that is over ten times higher than at RHIC. Among the six experiments at LHC, A Large Ion Collider Experiment (ALICE) is dedicated to heavy-ion physics. Also CMS and ATLAS have active heavy-ion programs.

The first indisputable evidence of QGP came from RHIC [1] measurements in 2004. Originally it was believed that QGP behaves as an ideal gas. The first hints against the ideal gas assumption came from Lattice QCD calculations [32] which showed that QGP approaches the Stefan-Boltzmann limit very slowly and the RHIC observations confirmed that QGP behaves more like a strongly interacting fluid. i.e. it has no or very little viscosity. This discovery strengthened the role

of hydrodynamics [41–43] as a way of describing collective (low p_{T}) phenomena in heavy-ion physics. I will discuss the hydrodynamical approach in section 2.2. Another approaches into modelling heavy-ion collisions have been successful. In this thesis I will study A MultiPhase Transport (AMPT) model, which is a hybrid model. Unlike hydrodynamics the model treats particles and their interactions individually with the use of Monte Carlo simulations.

QGP has also provided string theorists a long sought-after method to test dynamics of strongly-coupled gauge theory [44], since it seems that the viscosity of the QGP is very small and might be very close to a lower bound of shear viscosity to entropy ratio η/s suggested by string theoretical calculations[1]. According to the calculations η/s, has an universal minimum value of $\hbar/4\pi k_B$ [46]. This universal minimum value of $1/4\pi \approx 0.08$, would hold for all substances. According to the theory the limit could be reached in the strong coupling limit of gauge theories and the limit in QCD is QGP.

The ratio η/s of QGP can not be directly measured but it can be estimated with data from heavy-ion collisions. Comparing hydrodynamical calculations with different η/s values to experimental data gives an estimate of the η/s in the system. The minimum value of η/s is found in the vicinity of the critical temperature, T_c [47]. Finding the η/s values in QGP matter would therefore also provide a way of determining the critical point of QCD matter [47]. At RHIC [47] the ratio has been constructed from v_2 measurements. The estimated ratio in QGP and temperature dependance of the ratio in different substances is shown in Fig.3.

The η/s value for the matter created in Au-Au collisions at RHIC ($\sqrt{s_{NN}} =$ 200 GeV) has been estimated to be 0.09 ± 0.015 [47], which is very close to the predicted lowest value. This suggests that the the matter created goes through a phase where it is close to the critical point of QCD.

[1]One should note that finite minimal viscosity was discussed by Gyulassy and Danielewicz already in 1980's [45], a long before any string theoretical calculations.

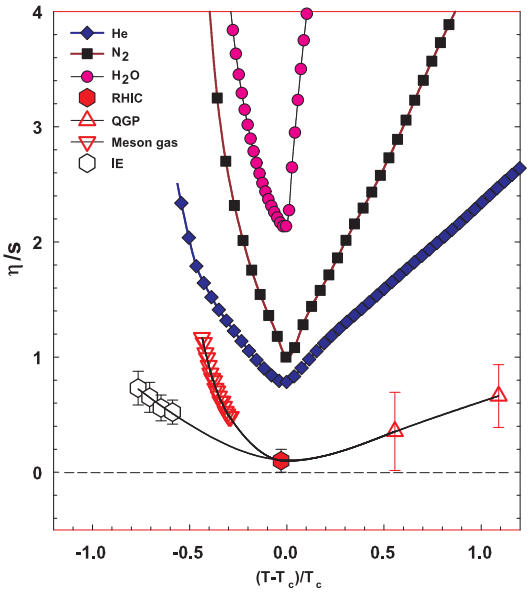

Figure 3: η/s as a function of $(T - T_c)/T_c$ for several substances as indicated. The calculated values for the meson-gas have an associated error of $\sim 50\%$ The lattice QCD value $T_c = 170$ MeV is assumed for nuclear matter. The lines are drawn to guide the eye. [47]

2 Features of Heavy-Ion Collisions

2.1 Collision Geometry

In contrast to protons atomic nuclei are objects with considerable transverse size. The properties of a heavy-ion collision depend strongly on the impact parameter b which is the vector connecting the centers of the two colliding nuclei at their closest approach. One illustration of a heavy-ion collision is shown in Fig. 4.

Impact parameter defines the reaction plane which is the plane spanned by b and the beam direction. Ψ_{RP} gives the angle between the reaction plane and some reference frame angle. Experimentally the reference frame is fixed by the detector setup. Reaction plane angle cannot be directly measured in high energy nuclear collisions, but it can be estimated with the event plane method [48].

Participant zone is the area containing the participants. The distribution of nucleons in the nucleus exhibits time-dependent fluctuations. Because the nucleon distribution at the time of the collision defines the participant zone, the axis of the participant zone fluctuates and can deviate from the reaction plane. The angle between the participant plane and the reaction plane is defined by [50]

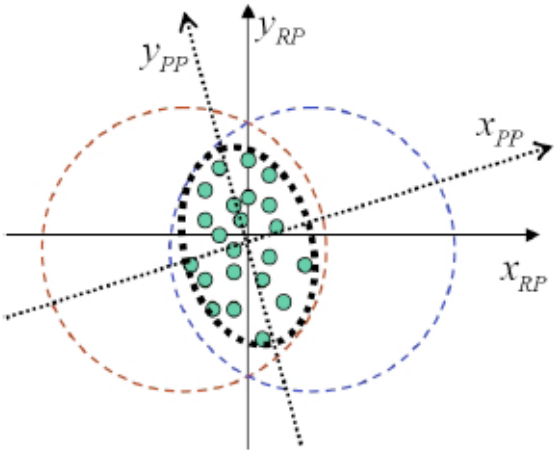

Figure 4: The definitions of the Reaction Plane and Participant Plane coordinate systems [49]. The dashed circles represent the two colliding nuclei and the green dots are partons that take part in the collision. x_{PP} and x_{RP} are the participant and reaction planes. The angle between x_{RP} and x_{PP} is given by Eq. (4). y_{PP} and y_{RP} are lines perpendicular to the participant and reaction planes.

$$\psi_{PP} = \arctan \frac{-2\sigma_{xy}}{\sigma_y^2 - \sigma_x^2 + \sqrt{\left(\sigma_y^2 - \sigma_x^2\right)^2 + 4\sigma_{xy}^2}}, \tag{4}$$

where the σ-terms are averaged over the energy density.

$$\sigma_y^2 = \langle y^2 \rangle - \langle y \rangle^2, \sigma_x^2 = \langle x^2 \rangle - \langle x \rangle^2, \sigma_{xy} = \langle xy \rangle - \langle x \rangle \langle y \rangle \tag{5}$$

The impact parameter is one way to quantize the centrality of a heavy-ion collision but it is impossible to measure in a collision. It can be estimated from observed data using theoretical models, but this is always model-dependent and to compare results from different experiments one needs an universal definition for centrality. The difference between central and peripheral collisions is illustrated in Fig. 5. In a central collision the overlap region is larger than in a peripheral collision. Larger overlap region translates into a larger number of nucleons participating in the collision, which in turn leads to a larger number of particles produced in the event.

Usually centrality is defined by dividing collision events into percentile bins by the number participants or experimentally by the observed multiplicity. Centrality bin 0-5% corresponds to the most central collisions with the highest multiplicity and higher centrality percentages correspond to more peripheral collisions with lower multiplicities. A multiplicity distribution from ALICE measurements [51]

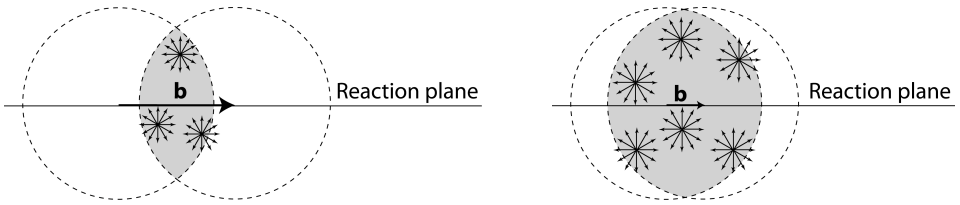

(a) Peripheral collision (b) Central collision

Figure 5: Interaction between partons in central and peripheral collisions. The snowflakes represent elementary parton-parton collisions. When the impact parameter b is large the number of elementary collisions is small. Particle production is small. Smaller impact parameter increases the number of elementary collisions. This increases particle production.

illustrating the centrality division is shown in Fig. 6. The distribution is fitted using a phenomenological approach based on a Glauber Monte Carlo [52] plus a convolution of a model for the particle production and a negative binomial distribution.

2.1.1 Nuclear Geometry

To model heavy-ion collisions one must first have a description as good as possible of the colliding objects. Atomic nuclei are complex ensembles of nucleons. The nuclei used in heavy-ion physics have in the order of 200 nucleons. Mostly used nuclei are ^{208}Pb at LHC and ^{197}Au at RHIC. The distribution of these nucleons within a nucleus is not uniform and is subject to fluctuations in time.

Nuclear geometry in heavy-ion collisions is often modelled with the Glauber Model. The model was originally developed to address the problem of high energy scattering with composite particles. Glauber presented his first collection of papers and unpublished work in his 1958 lectures [53]. In the 1970's Glauber's work started to have utility in describing total cross sections. Maximon and Czyz applied it to proton-nucleus and nucleus-nucleus collisions in 1969 [54].

In 1976 [55] Białłas, Bleszyński, and Czyż applied Glauber's approach to inelastic nuclear collisions. Their approach introduced the basic functions used in modern language including the thickness function and the nuclear overlap function. Thickness function is the integral of the nuclear density over a line going through the nucleus with minimum distance s from its center

$$T_A(s) = \int_{-\infty}^{\infty} \mathrm{d}z \rho\left(\sqrt{s^2 + z^2}\right). \tag{6}$$

This function gives the thickness of the nucleus, i.e. the amount material seen by a particle passing through it.

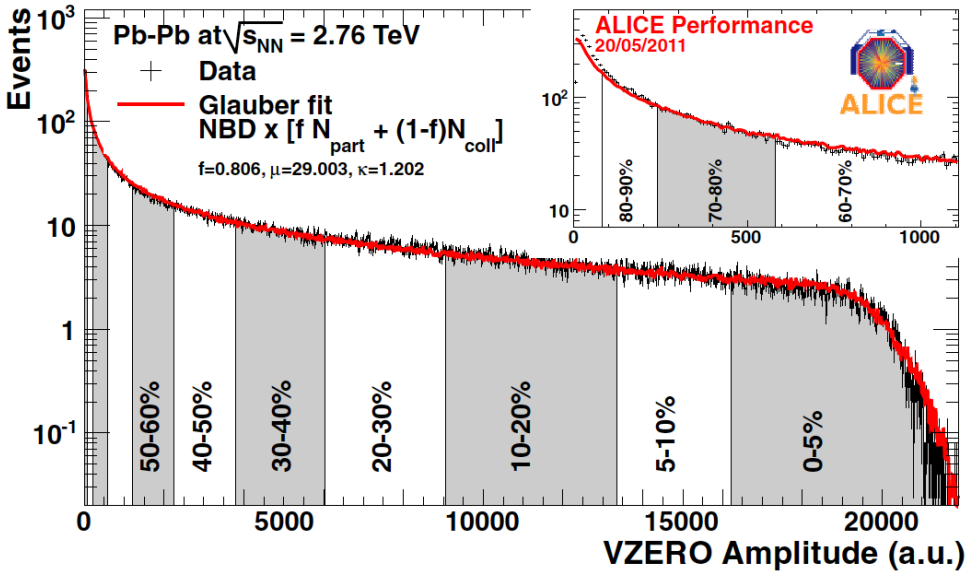

Figure 6: An illustration of the multiplicity distribution in ALICE measurements. The red line shows the fit of the Glauber calculation to the measurement. The data is divided into centrality bins [51]. The size of the bins corresponds to the indicated percentile.

Overlap function is an integral of the thickness functions of two colliding nuclei over the overlap area. This can be seen as the material that takes part in the collision. It is given as a function of the impact parameter b

$$T_{AB}(b) = \int \mathrm{d}s^2 T_A(\bar{s})\, T_B\left(\bar{s} - \bar{b}\right) \tag{7}$$

The average overlap function, $\langle T_{AA} \rangle$, in an A-A collisions is given by [56]

$$\langle T_{AA} \rangle = \frac{\int T_{AA}(b)\ \mathrm{d}b}{\int \left(1 - e^{-\sigma_{pp}^{inel} T_{AA}(b)}\right)\ \mathrm{d}b}. \tag{8}$$

Using $\langle T_{AA} \rangle$ one can calculate the mean number of binary collisions

$$\langle N_{coll} \rangle = \sigma_{pp}^{inel} \langle T_{AA} \rangle, \tag{9}$$

where the total inelastic cross-section, σ_{pp}^{inel}, gives the probability of two nucleons interacting. The number of binary collisions is related to the hard processes in a heavy-ion collision. Each binary collision has equal probability for direct production of high-momentum partons. Thus the number of high momentum particles is proportional to $\langle N_{coll} \rangle$.

Soft production on the other hand is related to the number of participants. It is assumed that in the binary interactions participants get excited and further interactions are not affected by previous interactions because the time scales are too short for any reaction to happen in the nucleons. After the interactions excited nucleons are transformed into soft particle production. Production does not depend on the number of interactions a nucleon has gone through. The average number of participants, $\langle N_{part} \rangle$ can also be calculated from the Glauber model

$$\begin{aligned} \left\langle N_{part}^{AB}(b) \right\rangle &= \int \mathrm{d}s^2 T_A(\bar{s}) \left[1 - \left[1 - \sigma_{NN} \frac{T_B\left(\bar{s} - \bar{b}\right)}{B} \right]^B \right] \\ &+ \int \mathrm{d}s^2 T_B(\bar{s}) \left[1 - \left[1 - \sigma_{NN} \frac{T_A\left(\bar{s} - \bar{b}\right)}{A} \right]^A \right]. \end{aligned} \tag{10}$$

Glauber calculations require some knowledge of the properties of the nuclei. One requirement is the nucleon density distribution, which can be experimentally determined by studying the nuclear charge distribution in low-energy electron scattering experiments [52]. The nucleon density is usually parametrized by a Woods-Saxon distribution

$$\rho(r) = \frac{\rho_0}{1 + \exp\left(\frac{r-R}{a}\right)}, \tag{11}$$

where ρ_0 is the nucleon density in center of the nucleus, R is the nuclear radius and a parametrizes the depth of the skin. The density stays relatively constant as a function of r until around R where it drops to almost 0 within a distance given by a.

Another observable required in the calculations is the total inelastic nucleon-nucleon cross-section $\sigma_{\mathrm{inel}}^{\mathrm{NN}}$. This can be measured in proton-proton collisions at different energies.

There are two often used approaches to Glauber calculations. The optical approximation is one way to get simple analytical expressions for the nucleus-nucleus interaction cross-section, the number of interacting nucleons and the number of nucleon-nucleon collisions. In the optical Glauber it is assumed that during the crossing of the nuclei the nucleons move independently and they will be essentially undeflected.

With the increase of computational power at hand the Glauber Monte Carlo (GMC) approach has emerged as a method to get a more realistic description of the collisions. In GMC the nucleons are distributed randomly in three-dimensional coordinate system according to the nuclear density distributions. Also nuclear

parameters, like the radius R can be sampled from a distribution. A heavy-ion collision is then treated as a series of independent nucleon-nucleon collisions, where in the simplest model nucleons interact if their distance in the plane orthogonal to the beam axis, d, satisfies

$$d < \sqrt{\sigma_{\text{inel}}^{\text{NN}}} \tag{12}$$

The average number of participants and binary collisions can then be determined by simulating many nucleus-nucleus collisions. The results of one GMC Pb-Pb event with impact parameter $b = 9.8$fm is shown in Fig. 7

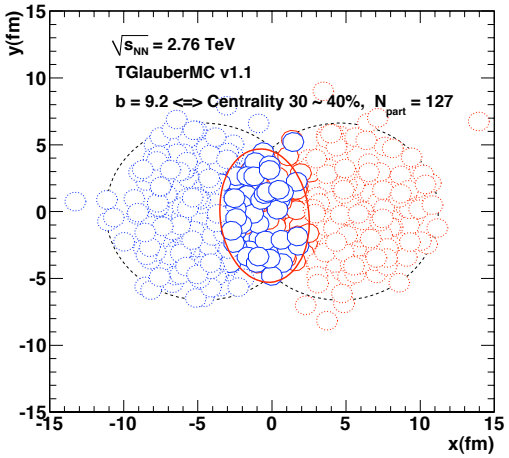

Figure 7: The results of one Glauber Monte Carlo simulation. Big circles with black dotted boundaries represent the two colliding nuclei. The participant zone is highlighted with the solid red line. Small red and blue circles represent nucleons. Circles with thick boundaries are participants i.e. they interact with at least one nucleon from the other nucleus. Small circles with dotted boundaries are spectators which do not take part in the collision.

2.2 Hydrodynamical Modelling

The relativistic version of hydrodynamics has been used to model the deconfined phase of a heavy-ion collision with success. Heavy-ion collisions produce many hadrons going into all directions. It is expected that tools from statistical physics would be applicable to this complexity [57]. The power of relativistic hydrodynamics lies in its simplicity and generality. Hydrodynamics only requires that there is local thermal equilibrium in the system. In order to reach thermal equilibrium the

system must be strongly coupled so that the mean free path is shorter than the length scales of interest [58].

The use of relativistic hydrodynamics in high-energy physics dates back to Landau [59] and the 1950's, before QCD was discovered. Back then it was used in proton-proton collisions. Development of hydrodynamics for the use of heavy-ion physics has been active since the 1980's, including Bjorken's study of boost-invariant longitudinal expansion and infinite transverse flow [41]. Major steps were taken later with the inclusion of finite size and and dynamically generated transverse size [42, 43], a part of which was done at the University of Jyväskylä. The role of hydrodynamics in heavy-ion physics was strengthened when QGP was observed to behave like a liquid by RHIC [1].

The evolution of a heavy-ion event can be divided into four stages. A schematic representation of the evolution of the collisions is shown in Fig. 8. Stage 1 follows immediately the collision. This is known as the pre-equilibrium stage. Hydrodynamic description is not applicable to this regime because thermal equilibrium is not yet reached. The length of this stage is not known but it is assumed to last about 1 fm/c in proper time τ.

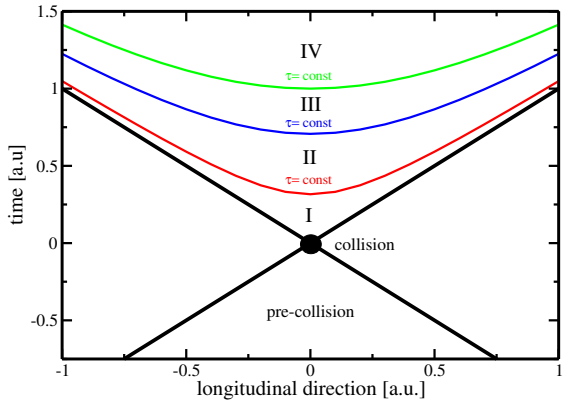

Figure 8: Schematic representation [58] of a heavy-ion collision as the function of time and longitudinal coordinates z The various stages of the evolution correspond to proper time $\tau = \sqrt{t^2 - z^2}$ which is shown as hyperbolic curves separating the different stages.

The second stage is the regime where thermal equilibrium or at least near-equilibrium is reached. In this stage hydrodynamics should be applicable if the temperature is above the deconfinement temperature [58]. This lasts about $5 - 10$ fm/c until the temperature of the system sinks low enough for hadronization to occur. Now the system loses its deconfined, strongly coupled, state and hydrodynamics can no longer be used. The third stage is the hadron gas stage where the hadrons still interact. This ends when hadron scattering becomes rare and they

no longer interact. In the final stage hadrons are free streaming and they fly in straight lines until they reach the detector.

The hydrodynamical approach treats the ensemble of particles as a fluid. It uses basic equations from hydrodynamics and thermodynamics but with a few modifications to account for the relativistic energies. The calculation is based on a collection of differential equations connecting the local thermal variables like temperature, pressure etc. to local velocities of the fluid. One also needs equations of state that connect the properties of the matter, e.g. temperature and pressure to density. Given initial conditions and equations of state the calculation gives the time-evolution of the system.

At first only ideal hydrodynamics was used. Ideal hydrodynamics does not include viscosity but it is a relatively good approximation and it could predict phenomena like elliptic flow. For more detailed calculations also viscosity must be considered and viscosity itself is an interesting property of QGP.

In this thesis I compare my results of identified particle flow to calculations from two hydrodynamical models; VISHNU model by Song *et al.* [60] and calculations by Niemi *et al.* [61].

2.3 Flow

In a heavy-ion collision the bulk particle production is known as flow. The production is mainly isotropic but a lot of studies including my thesis focus on the small anisotropies. After the formation of the QGP, the matter begins to expand as it is driven outwards by the strong pressure difference between the center of the collision zone and the vacuum outside the collision volume. The pressure-driven expansion is transformed into flow of low-momentum particles in the hadronization phase. Since the expansion is mainly isotropic the resulting particle flow is isotropic with small anisotropic corrections that are of the order of 10% at most. The isotropic part of flow is referred to as radial flow.

The transverse momentum spectra $\mathrm{d}N/\,\mathrm{d}p_\mathrm{T}$ in heavy-ion collisions is shown

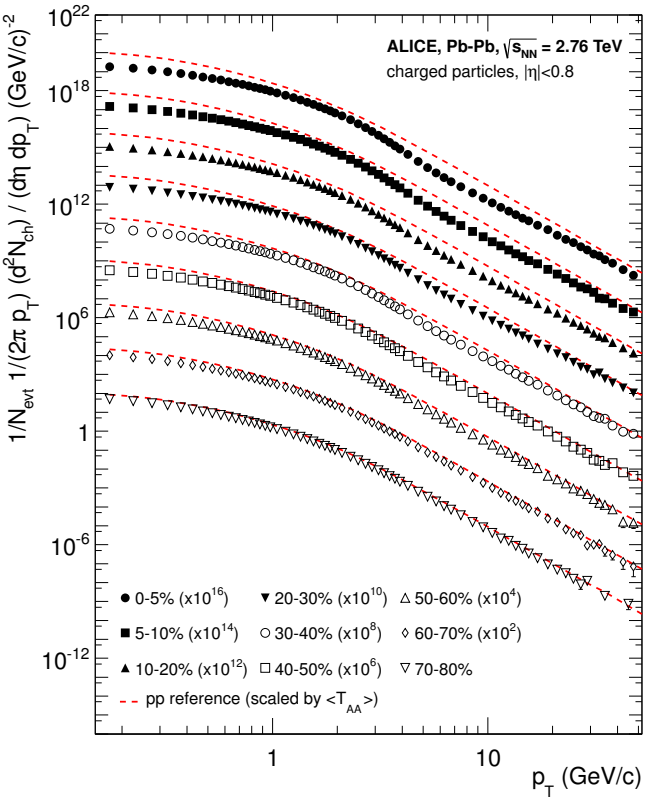

Figure 9: Charged particle spectra measured by ALICE [62] for the 9 centrality classes given in the legend. The distributions are offset by arbitrary factors given in the legend for clarity. The distributions are offset by arbitrary factors given in the legend for clarity. The dashed lines show the proton-proton reference spectra scaled by the nuclear overlap function determined for each centrality class and by the Pb-Pb spectra scaling factors [62].

in Fig. 9. The vast majority of produced particles have small p_{T}. The difference between the yield of 1 GeV/c and 4 GeV/c particles is already 2-3 orders of magnitude. Any observables that are integrated over p_{T} are therefore dominated by the small momentum particles.

2.3.1 Anisotropic Flow

In a non-central heavy-ion collision the shape of the impact zone is almond-like. In peripheral collisions the impact parameter is large which means a strongly asymmetric overlap region. In a central collision the overlap region is almost symmetric in the transverse plane. In this case the impact parameter is small. Collisions with different impact parameters are shown in Fig. 5.

The pressure gradient is largest in-plane, in the direction of the impact parameter b, where the distance from high pressure, at the collision center, to low pressure, outside the overlap zone, is smallest. This leads to stronger collective flow into in-plane direction, which in turn results in enhanced thermal emission through a larger effective temperature into this direction, as compared to out-of-plane [3, 4, 63]. The resulting flow is illustrated in Fig. 10. Flow with two maxima in the direction of the reaction plane is called elliptic flow. This is the dominant

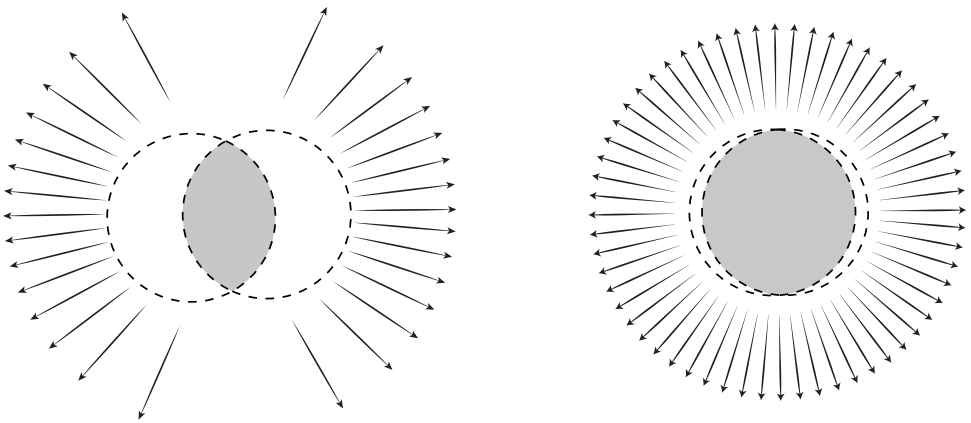

(a) Peripheral collision (b) Central collision

Figure 10: Illustration of flow in momentum space in central and peripheral collisions. The density of the arrows represent the magnitude of flow seen at a large distance from the collision in the corresponding azimuthal direction. In a peripheral collision momentum flow into in-plane direction is strong and flow into out-of-plane direction is weak. In a central collision anisotropy in flow is smaller, but the total yield of particles is larger.

part of anisotropic flow. Also more complex flow patterns can be identified. The most notable of these is the triangular flow, which is mainly due to fluctuations in the initial conditions.

Flow is nowadays usually quantified in the form of a Fourier composition

$$E\frac{\mathrm{d}^3N}{\mathrm{d}p^3} = \frac{1}{2\pi}\frac{\mathrm{d}^2N}{p_\mathrm{T}\,\mathrm{d}p_\mathrm{T}\,\mathrm{d}\eta}\left(1+\sum_{n=1}^{\infty}2v_n\left(p_\mathrm{T},\eta\right)\cos(n(\phi-\Psi_n))\right), \tag{13}$$

where the coefficients v_n give the relative strengths of different anisotropic flow components and the overall normalisation gives the strength of radial flow. Elliptic flow is represented by v_2 and v_3 represents triangular flow. The first coefficient, v_1, is connected to directed flow. This will however in total be zero because of momentum conservation. It can be nonzero in some rapidity or momentum regions but it must be canceled by other regions.

The first approaches to quantifying the anisotropy of flow did not use the Fourier composition. Instead they approached the problem with a classic event shape analysis using directivity [64] or sphericity [3, 65] to quantify the flow.

The first experimental studies of anisotropy were performed at the AGS [66] in 1993. They noted that the anisotropy of particle production in one region correlates with the reaction plane angle defined in another region.

The first ones to present the Fourier decomposition were Voloshin and Zhang in 1996 [67]. This new approach was useful for detecting different types of anisotropy in flow, since the different Fourier coefficients give different harmonics in flow. They also show the relative magnitude of each harmonic compared to radial flow.

Some parts of the Fourier composition approach were used for Au-Au collisions at $\sqrt{s_{NN}} = 11.4$ GeV at AGS in 1994 [68]. This analysis still focused on event shapes but they constructed these shapes using Fourier composition from different rapidity windows.

2.3.2 High p_T Phenomena

The measurement of anisotropic flow coefficients can be extended to very high transverse momenta p_T. High p_T measurements of v_2 from CMS [69] are shown in Fig. 11. For high transverse momenta v_2 values are positive and they decrease slowly as a function of p_T. At high transverse momentum the v_2 values don't, however, represent flow.

High momentum particles are very rare and they are only produced in the initial collisions. After they are created they escape the medium before a thermal equilibrium is reached. Thus they are not part of the pressure-driven collective expansion. Instead high momentum yield is suppressed because of energy loss in the medium. When propagating through the medium these partons lose energy as

they pass through the medium. This is referred to as jet quenching. Jet quenching depends on the path lengths through the medium. Thus anisotropy in this region is mainly dependent on the collision geometry and density of medium.

The energy loss of partons in medium is mainly due to QCD bremsstrahlung and to elastic scatterings between the parton and the medium.

In elastic scatterings the recoil energy of the scattered partons are absorbed by the thermal medium, which reduces the energy of the initial parton. The mean energy loss from elastic scatterings can be estimated by

$$\langle \Delta E \rangle_{el} = \sigma \rho L \langle E \rangle_{1scatt} \propto L, \tag{14}$$

where σ is the interaction cross section and $\langle E \rangle_{1scatt}$ is the mean energy transfer of one individual scattering [70].

Another energy loss mechanism is medium-induced radiation. In QCD this radiation is mainly due to the elementary splitting processes, $q \to qg_r$ and $g \to gg_r$. Assuming that the parton is moving with the speed of light radiation energy loss can be estimated by

$$\langle \Delta E \rangle_{rad} \propto T^3 L^2, \tag{15}$$

where L is the length of the medium and T is its temperature [71].

There are several models that attempt to describe the nature of the energy loss mechanism. The most used models can be divided into four formalisms.

In the Gyulassy-Levai-Vitev (GLV) [72] opacity expansion model the radiative energy loss is consiered on a few scattering centers N_{scatt}. The radiated gluon is constructed by pQCD calculation as summing up the relevant scattering amplitudes in terms of the number of scatterings. Another approach into opacity expansion is the ASW model by Armesto, Salgado and Wiedermann [73].

Thermal effective theory formulation by Arnold, Moore and Yaffe (AMY) [74] uses dynamical scattering centers. It is based on leading order pQCD hard thermal loop effective field theory. This model assumes that because of the high temperature of the plasma the strong coupling constant can be treated as small. The parton propagating through the medium will lose energy from soft scatterings and hard scatterings.

The above models calculate the energy loss while the parton propagates through the medium, focusing on the pQCD part. The higher twist (HT) approach by Wang and Guo [75] implements the energy loss mechanism in the energy scale evolution of the fragmentation functions.

The last category is formed by the Monte Carlo methods. The PYTHIA event generator [76] is widely used in high-energy particle physics. Two Monte Carlo models based on PYTHIA describing the energy loss mechanism are PYQUEN [77]

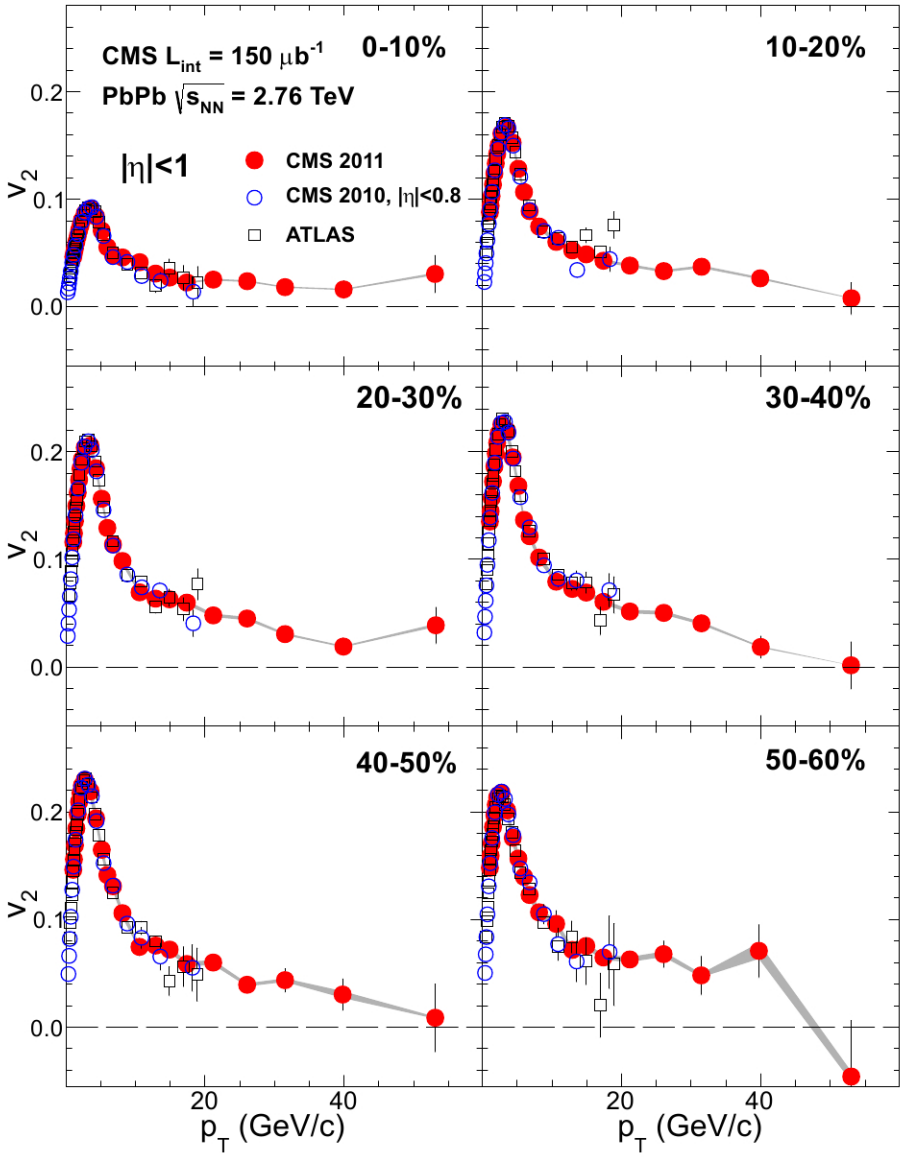

Figure 11: Elliptic flow, v_2, as a function of the charged particle transverse momentum from 1 to 60 GeV/c with $|\eta| < 1$ for six centrality ranges in Pb-Pb collisions at $\sqrt{s_{NN}} = 2.76$ TeV, measured by the CMS experiment. [69].

and Q-Pythia [78]. Other Monte Carlo models include JEWEL [79] and YaJEM [80].

Jet quenching in heavy-ion collisions is usually quantized with the nuclear modification factor R_{AA}, which is is defined as

$$R_{AA}\left(p_{\mathrm{T}}\right) = \frac{\left(1/N_{AA}^{evt}\right) \mathrm{d}N^{AA}/\,\mathrm{d}p_{\mathrm{T}}}{\langle N_{coll}\rangle \left(1/N_{pp}^{evt}\right) \mathrm{d}N^{pp}/\,\mathrm{d}p_{\mathrm{T}}} \tag{16}$$

where $\mathrm{d}N^{AA}/\,\mathrm{d}p_{\mathrm{T}}$ and $\mathrm{d}N^{pp}/\,\mathrm{d}p_{\mathrm{T}}$ are the yields in heavy-ion and proton-proton collisions, respectively and $\langle N_{coll}\rangle$ is the average number of binary nucleon-nucleon collisions in one heavy-ion event. The number of binary collisions can be calculated from the Glauber model as shown in Sec. 2.1.1. From the point of view of direct production a heavy-ion collision can be estimated relatively well to be only a series of proton-proton collisions.

If the medium has no effect on high p_{T} particles the nuclear modification factor should be 1. At RHIC and LHC this has been observed to be as low as 0.2 because of jet quenching. Measurements of R_{AA} from different sources are shown in Fig. 12

The nuclear modification factor can also be used to quantify anisotropy. In the study of anisotropy R_{AA} in-plane and out-of-plane can be compared. The distance traveled through medium is largest out-of-plane which leads to stronger suppression in this direction. The nuclear modification factor as a function of $\Delta\phi = \phi - \psi_n$ is given by

$$\begin{aligned} R_{AA}\left(\Delta\phi, p_{\mathrm{T}}\right) &= \frac{\left(1/N_{AA}^{evt}\right) \mathrm{d}^2N^{AA}/d\Delta\phi\,\mathrm{d}p_{\mathrm{T}}}{\langle N_{coll}\rangle \left(1/N_{pp}^{evt}\right) \mathrm{d}N^{pp}/\,\mathrm{d}p_{\mathrm{T}}} \approx \frac{\mathrm{d}N^{AA}/\,\mathrm{d}p_{\mathrm{T}}\left(1 + 2\cdot v_2\cos\left(2\Delta\phi\right)\right)}{\langle N_{coll}\rangle\ \mathrm{d}N^{pp}/\,\mathrm{d}p_{\mathrm{T}}} \\ &= R_{AA}^{incl}(p_{\mathrm{T}})\left(1 + 2\cdot v_2\cos\left(2\Delta\phi\right)\right). \end{aligned} \tag{17}$$

The yield of proton-proton collisions is independent of the reaction plane and the yield in heavy-ion collisions is modulated by the second harmonics. In Eq. (17) R_{AA} is approximated only up to the second harmonics. From Eq. (17) it follows that

$$\frac{R_{AA}\left(0, p_{\mathrm{T}}\right) - R_{AA}\left(\pi/2, p_{\mathrm{T}}\right)}{R_{AA}^{incl}(p_{\mathrm{T}})} \approx \frac{R_{AA}^{incl}(p_{\mathrm{T}})\left(1 + 2\cdot v_2 - (1 - 2\cdot v_2)\right)}{R_{AA}^{incl}(p_{\mathrm{T}})} = 4\cdot v_2 \tag{18}$$

The observed $R_{AA}\left(\Delta\phi, p_{\mathrm{T}}\right)$ from PHENIX measurements in Au-Au collisions at $\sqrt{s} = 200$ GeV [92] is compared to R_{AA} using v_2 via Eq. (17) in Fig. 13. They agree very well within the statistical errors for all centrality and p_{T} bins.

At high-p_{T}, the pQCD processes are dominant, hence the v_n (or $R_{AA}(\Delta\phi, p_{\mathrm{T}})$) characterize the pathlength-dependence of the energy loss process.

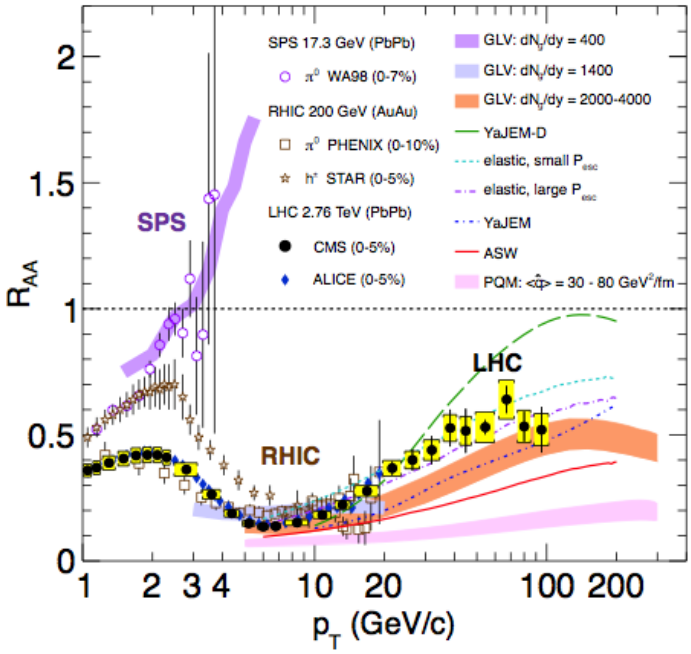

Figure 12: Measurements of the nuclear modification factor R_{AA} in central heavy-ion collisions at three different center-of-mass energies, as a function of p_{T}, for neutral pions (π^0), charged hadrons ($h\pm$), and charged particles [81–85], compared to several theoretical predictions [36, 86–90]. The error bars on the points are the statistical uncertainties, and the yellow boxes around the CMS points are the systematic uncertainties. The bands for several of the theoretical calculations represent their uncertainties [91].

Jet quenching is not the only high p_{T} phenomenon studied in heavy-ion collisions. Another property is jet fragmentation. The high momentum parton created in the initial collision fragments into a number of partons with smaller p_{T}. Jet fragmentation occurs also in proton-proton collisions in the vacuum, but it can be modified due to the presence of the medium. In order to study the jet fragmentation function ($D(z)$, where $z = p_{\mathrm{T}}^{h}/p_{\mathrm{T}}^{part}$) modification due the medium, we use the two-particle correlations. The particle yield can be extracted from the correlation function. The background from the flow processes is correlated and needs to be subtracted to get the particle yield associated only with the jet. The ratio of the jet yields in Au-Au and p-p collision $I_{AA} = Y^{Au+Au}/Y^{p+p}$ characterizes the jet fragmentation modification [93]. I_{AA} probes the interplay between the parton production spectrum, the relative importance of quark-quark, gluon-gluon and quark-gluon final states, and energy loss in the medium.

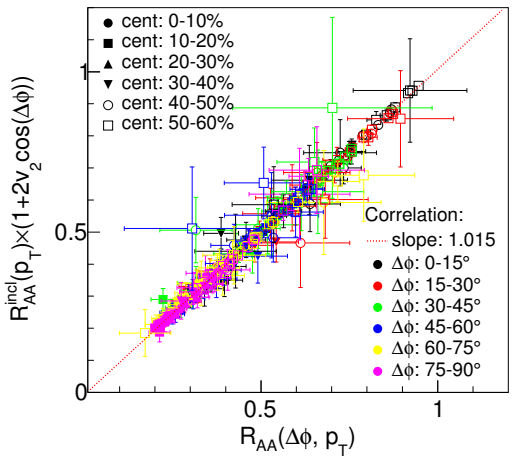

Figure 13: A comparison between observed $R_{AA}(\Delta\phi, p_{\mathrm{T}})$ and R_{AA} using v_2 from PHENIX measurements of Au-Au collisions at $\sqrt{s} = 200$ GeV. On the X-axis is the measured $R_{AA}(\Delta\phi, p_{\mathrm{T}})$. On the y-axis is the inclusive R_{AA} multiplied by $1 + 2v_2 \cos(\Delta\phi)$ [92].

2.3.3 Fluctuations and Event-by-Event Flow

The colliding nuclei are not static objects but the distribution of nucleons fluctuates over time. The arrangement of the nucleons at the time of the collision is random, which leads to fluctuations in the initial conditions. The shape of the collision zone is not a perfect almond and it can have a more complex shape. Also the density of the created medium is not homogenous but it can have dense hot spots. The initial density distribution of the created medium is the main reason for anisotropic flow. Because of fluctuations the strength of anisotropic flow is not constant event-by-event.

The existence of more complex density profiles also leads to odd flow harmonics. The basic hydrodynamical approach could only explain elliptic flow and even-harmonics. For a long time it was believed that the odd harmonics would be negligible. In 2007 Mishra *et* al. [94] argued that density inhomogeneities in the initial state would lead to non-zero v_n values for higher harmonics including v_3. It was later noted that higher harmonics of v_n would be suppressed by viscous effects and that the shape of v_n as a function of n would provide another valuable tool for studying η/s [95].

In 2010 significant v_3 components were also observed in RHIC data [96]. The AMPT model that is also studied in this thesis was able to quantitatively describe the centrality dependence of v_3 at RHIC and LHC energies, $\sqrt{s_{NN}} = 200$ GeV and

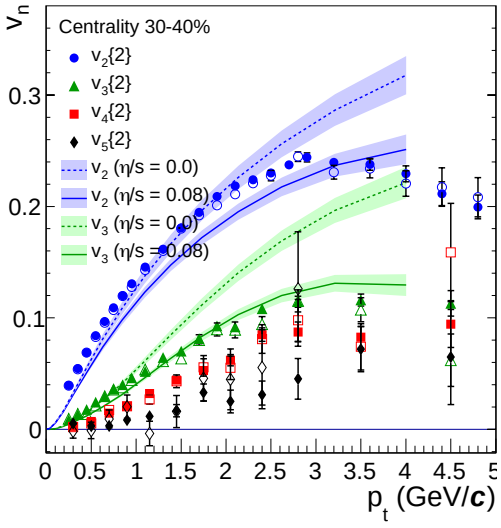

(a) ALICE measurement of v_2, v_3, v_4, v_5 as a function of transverse momentum. The flow coefficients are determined by two-particle correlations using different rapidity separations. The full and open symbols are for $\Delta\eta > 0.2$ and $\Delta\eta > 1.0$. The results are compared to hydrodynamic predictions [101] with different values of η/s [99].

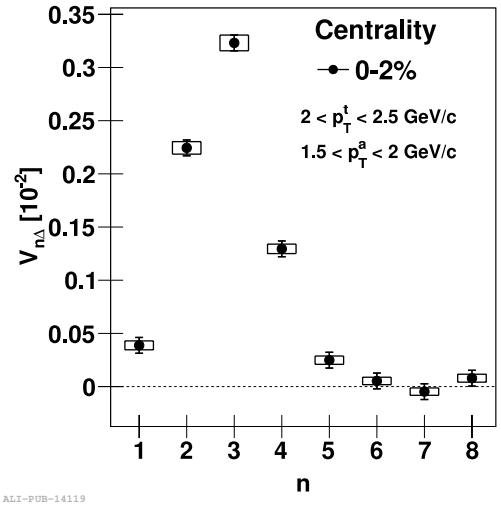

(b) Amplitude of v_n harmonics as a function of n for the 2% most central collisions as measured by ALICE [100].

Figure 14: Flow measurements of higher harmonics

2.76 TeV [97].

Contrary to elliptic flow higher harmonics are not strongly affected by the centrality of the collision. This supports the theory of higher harmonics being the result of fluctuations. Also v_2 measurements of ultra-central collisions give non-zero results for flow, even though the traditional approach based on the anisotropy of the overlap zone gives no prediction of anisotropic flow. This is also the result of fluctuations. Measurement of distributions of v_n coefficients has been performed at ATLAS [98]. Their measurements of distributions for v_2 in central collisions and for v_3 and v_4 in general are consistent with a pure Gaussian fluctuation scenario [98].

Measurements of different flow harmonics are shown in Fig. 14. The left panel shows different flow harmonics as a function of p_{T} as measured by ALICE [99] in peripheral collisions. In general flow coefficients decrease as a function of n after $n = 2$. Central collisions are an exception.The right panel of Fig. 14 shows v_n as a function of n in central collisions as measured by ALICE [100].

Measurement of event-by-event flow and higher harmonics has growing importance in the field. Triangular flow is useful also for studying jet quenching and in-medium energy loss since anisotropies of flow are related to the path lengths of partons traversing through the medium. Path-lengths and medium density in turn are related the energy loss. An interesting topic of future research would be studying jet properties like R_{AA} separately in events with strong and weak anisotropy.

2.4 Identified Charged Particle Flow

In this thesis I study flow of identified charged particles in the AMPT model. Analysis of identified flow has been performed already at RHIC and now at LHC. The ALICE detector at LHC has unique particle identification capabilities. This makes it well suited to measuring flow of identified particles [102]. Results from ALICE for spectra of pions, kaons and protons are shown in Fig. 15. The experimental results are overlaid with hydrodynamical calculations from the VISHNU model [60]. The figure shows that vast majority of hadrons produced in a heavy-ion collision are pions. The yield of pions is an order of magnitude larger than the yield of kaons and almost three orders larger than the yield of protons. Pions are the lightest of hadrons (mass of $\pi^{\pm} \approx 140$ MeV/c) which makes producing them more favourable than production of protons (mass ≈ 938 MeV/c).

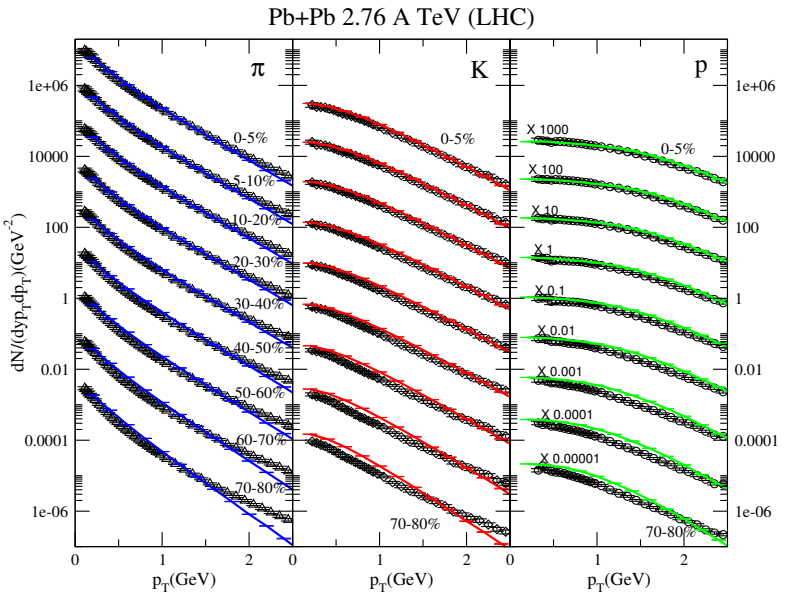

Figure 15: Transverse momentum spectra for pions, kaons and protons in $\sqrt{s_{NN}} =$ 2.76 TeV Pb-Pb collisions. Experimental data are from ALICE [102]. Theoretical curves are from hydrodynamical calculations [60]. From top to bottom the curves correspond to 0-5% ($\times$1000), 5-10% ($\times$100), 10-20% ($\times$10), 20-30%, 30-40% ($\times$0.1), 40-50% ($\times$0.01), 50-60% ($\times$0.001), 60-70% ($\times 10^{-4}$), 70-80% ($\times 10^{-5}$) centrality, respectively, where the factors in parentheses indicate the multipliers applied to the spectra for a more clear presentation [60].

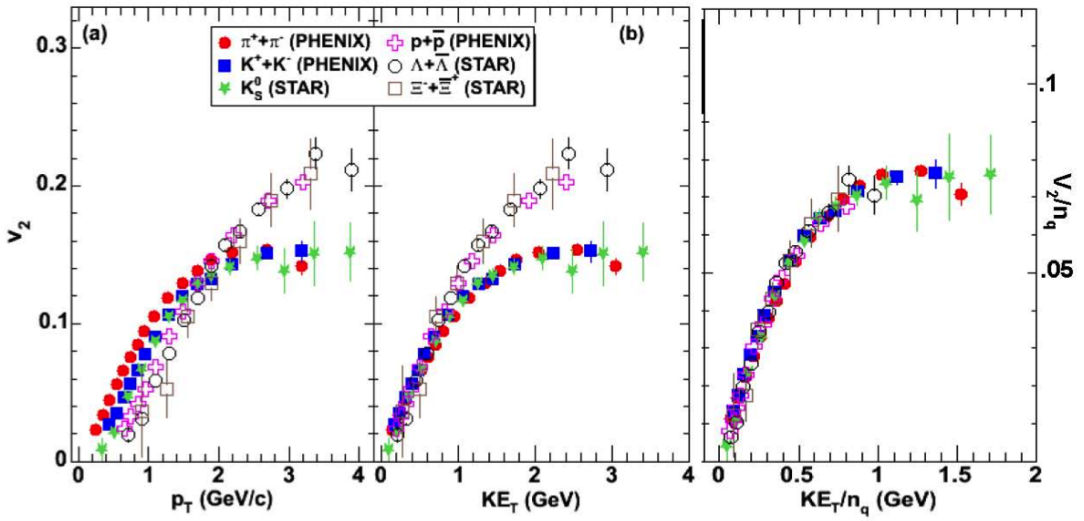

Figure 16: (a) v_2 as a function of p_{T}, (b) v_2/n_q as a function of p_{T}/n_q and (right) v_2/n_q as a function of KE_T/n_q for identified particle species obtained in minimum bias Au-Au collisions [103].

2.4.1 Quark Number Scaling

Anisotropic flow studies can be extended to identified particles. When studying elliptic flow coefficients of different particle species as a function of p_{T} one sees that the data are ordered by the masses of the particles. There is also a clear separation between mesons and baryons. Scaling v_n coefficients by the number of quarks, n_q (For mesons $n_q = 2$ and for baryons $n_q = 3$) removes this separation. Results from v_2 measurements in Au-Au collisions at $\sqrt{s_{NN}} = 200$ GeV from PHENIX [103] are shown in Fig. 16. At RHIC it was further observed that plotting the coefficients as a function of transverse kinetic energy KE_T

$$KE_T = \sqrt{m^2 + p_{\mathrm{T}}^2} - m \tag{19}$$

instead of p_{T} removes the mass ordering and gives almost perfect scaling between identified hadrons. Differences vanish in some energy range completely [103]. This was taken as a strong indication that anisotropic flow at RHIC develops primarily in the partonic phase, and is not strongly influenced by the subsequent hadronic phase [8].

Particle specific flow has also been studied in ALICE at LHC with $\sqrt{s_{NN}} =$ 2.76 TeV [8]. It has been observed that the quark number scaling that worked perfectly at RHIC breaks down at LHC energies. Pions and kaons align well, but proton $v_2/n_q\,(KE_T)$ data does not follow the meson data. Data from ALICE is shown in Fig. 17.

One way to get similar scaling also for protons was presented by Lacey *et al* [8]. They assumed that proton data had a blueshift of 0.2 GeV/c and correcting this with a similar redshift, i.e. decreasing the proton p_{T} by 0.2 GeV/c prior to the quark number scaling almost restores the scaling between protons and light mesons.

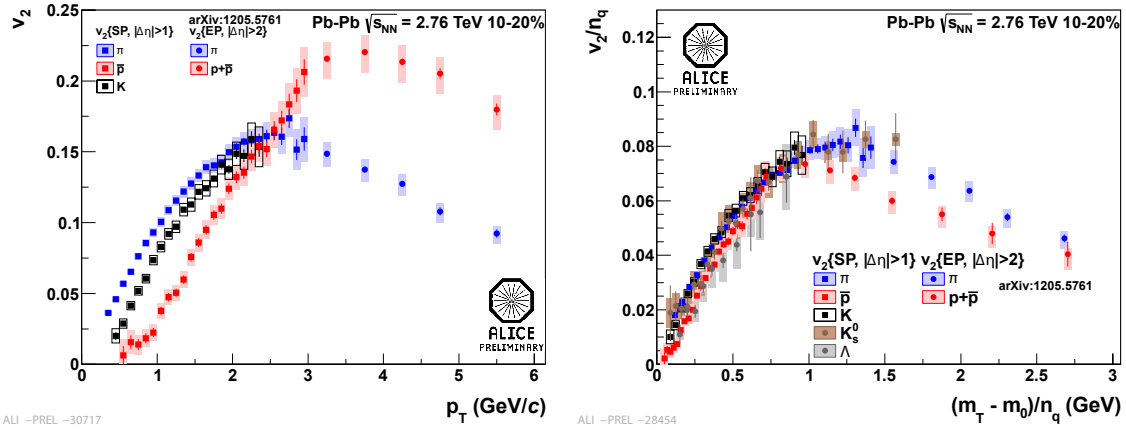

Figure 17: Identified particle flow coefficients with quark number scaling as measured by ALICE.

2.4.2 Quark Coalescence Model

Quark number scaling has been explained by a simple quark coalescence model, with constituent quark recombination [104]. Since v_2 is the coefficient from a Fourier series it can be calculated for quarks by

$$v_{2,q} = \langle \cos(2\phi) \rangle = \frac{1}{2\pi} \int_0^{2\pi} \frac{\mathrm{d}N^{quark}}{\mathrm{d}\phi} \cos(2\phi)\, \mathrm{d}\phi, \tag{20}$$

In the coalescence model the hadronization phase is described such that three nearest quarks combine into a baryon and nearby quark-antiquark pairs combine into mesons. The usual coalescence model assumes that the invariant spectrum of particles produced in the hadronization is proportional to the product of the invariant spectra of constituents, i.e. the quarks [104]. In this case the Baryon N_b and meson N_m spectra are given by

$$\begin{aligned} \frac{\mathrm{d}N_b}{\mathrm{d}^2 p_{\mathrm{T}}}(p_{\mathrm{T}}) &= C_b(p_{\mathrm{T}}) \left[\frac{\mathrm{d}N_q}{\mathrm{d}^2 p_{\mathrm{T}}} \left(\frac{p_{T,q}}{3} \right) \right]^3 \\ \frac{\mathrm{d}N_m}{\mathrm{d}^2 p_{\mathrm{T}}}(p_{\mathrm{T}}) &= C_m(p_{\mathrm{T}}) \left[\frac{\mathrm{d}N_q}{\mathrm{d}^2 p_{\mathrm{T}}} \left(\frac{p_{T,q}}{2} \right) \right]^2, \end{aligned} \tag{21}$$

where the coefficients C_b and C_m are probabilities for $q\bar{q}$ to meson and qqq to baryon coalescence. Hence the meson and baryon v_2 coefficients are

$$v_{2,h} = \frac{1}{2\pi}\int_0^{2\pi}\left(\frac{\mathrm{d}N^{quark}}{\mathrm{d}\phi}\right)^{n_q}\cos\left(2\phi\right)\,\mathrm{d}\phi = n_q v_{2,q}. \tag{22}$$

where n_q is the number of quarks. Therefore

$$\begin{aligned} v_{2,m}\left(KE_T\right) &\approx 2\cdot v_{2,q}\left(\frac{KE_T}{2}\right), \\ v_{2,b}\left(KE_T\right) &\approx 3\cdot v_{2,q}\left(\frac{KE_T}{3}\right) \end{aligned} \tag{23}$$

Identified charged particle flow at LHC energies has also been studied in hydrodynamical calculations. For example in the VISHNU model [60]. The model has provided similar results as the LHC measurements.

The simple quark coalescence model has been challenged and nowadays many believe that there is actually no reason for perfect quark number scaling. So far there is no agreement of what causes the breaking of quark number scaling at LHC energies or why it worked so well for RHIC data.

The AMPT model that I study in thesis uses the simple quark coalescence assumption in the hadronization phase. Therefore it should give perfect quark number scaling. I will present results of identified particle flow and quark number scaling in the model.

3 Methodology

I will now explain the basic principles and methods I use in this thesis concerning the determination of flow coefficients. I study only simulated data but these methods are used also for real experimental data. There are several ways of calculating the v_n coefficients. In this thesis I use the event plane method for the identified charged particle flow coefficients which are averaged over events. For event-by-event flow I use another method that is explained in section 3.2.

3.1 Event Plane Method

The azimuthal angle dependence of the invariant yield, as a function of p_{T} and rapidity y, can be expressed using Fourier series as

$$E\frac{\mathrm{d}^3N}{\mathrm{d}p^3} = \frac{1}{2\pi}\frac{\mathrm{d}^2N}{p_{\mathrm{T}}\mathrm{d}p_{\mathrm{T}}\mathrm{d}y}\left(1+\sum_{n=1}^{\infty}2v_n\left(p_{\mathrm{T}},y\right)\cos(n(\phi-\psi_n))\right), \tag{24}$$

where the v_n coefficients are the flow coefficients. They also depend on p_{T} and y. Event plane method uses event plane angles ψ_n to calculate these coefficients. Event planes, unlike the reaction plane, depend on n and are only defined by the Fourier series.

The first step is the calculation of the event flow vector Q_n, which is defined as

$$\begin{aligned} Q_{n,x} &= \sum_i w_i\cos(n\phi_i) = Q_n\cos(n\psi_n), \\ Q_{n,y} &= \sum_i w_i\sin(n\phi_i) = Q_n\sin(n\psi_n). \end{aligned} \tag{25}$$

We sum over all particles used in determination of the event plane (i index). w_i is the weight for particle i and ϕ_i is its azimuthal angle in the laboratory frame. In this study there is no weighting and $w_i = 1$. When using weighting the weight w_i should approximate $v_n(p_{\mathrm{T}},y)$. For low transverse momentum $v_n(p_{\mathrm{T}},y)$ increases almost linearly with p_{T} [48]. The transverse momentum is therefore a good and common choice as weight. The difference between using unity or weighting with p_{T} is small [105].

One gets the event plane angle from Q_n

$$\psi_n = \frac{1}{n}\arctan\left(\frac{Q_{n,y}}{Q_{n,x}}\right). \tag{26}$$

The observed v_n is given by the average over azimuthal angles of all particles of a single type in an event in a given pseudorapidity and transverse momentum space bin

$$v_n^{obs}(p_{\mathrm{T}}, \eta) = \langle \cos[n(\phi_i - \psi_n)] \rangle. \tag{27}$$

One must be careful not to use the particles that were used in sums (25) to calculate v_n. Otherwise this leads to auto-correlations. In this thesis this is avoided by using forward particles to calculate the event plane angles and mid-rapidity particles to calculate v_n coefficients.

Finite multiplicity limits the estimation of the event plane angle. If there is a difference between the measured event plane and the true event plane, i.e. $\psi_n - \psi_n^{\mathrm{true}} \neq 0$ the observed flow coefficient changes. This must be corrected with the event plane resolution which is defined as

$$\mathcal{R}_n = \langle \cos[n(\psi_n - \psi_n^{\mathrm{true}})] \rangle, \tag{28}$$

where the average is taken over a large number of events [50]. Although $\mathcal{R}_n$ is not constant event-by-event, only the average value is often used. In an ideal case one would use event-by-event resolutions but in practice this is more challenging. The resolution depends on strength of flow and available statistics. Stronger flow makes the estimation of event planes more accurate. Thus with more multiplicity or larger v_n coefficients the resolution is larger.

This resolution formula requires that one knows the actual event plane angle ψ_n^{true}. This is possible in simulations, but in real experiments this has to be modified to work without ψ_n^{true}.

The final flow coefficients are given by the resolution correction

$$v_n = \frac{v_n^{obs}}{\mathcal{R}_n}. \tag{29}$$

3.1.1 Event Plane Resolution from Two Sub Event Method

In general the true event plane angle is not known. Therefore the event plane resolution has to be estimated using alternative methods. An estimate can be done by dividing the full event into two subevents.

For the two-subevent method one must have two symmetric detectors or two subsets with the same multiplicities from an event. In this method the event plane resolution can be expressed as a function of the resolution parameter χ, which is a function of v_n and the multiplicity, N [48]

$$\chi = v_n \sqrt{N}, \tag{30}$$

$$\mathcal{R}_n = \langle \cos(n(\psi_n - \psi_n^{\mathrm{true}})) \rangle = \frac{\sqrt{\pi}}{2} \chi e^{-\frac{\chi^2}{2}} \left[I_{\frac{n-1}{2}} \left(\frac{\chi^2}{2} \right) + I_{\frac{n+1}{2}} \left(\frac{\chi^2}{2} \right) \right], \tag{31}$$

where I is the modified Bessel function of the first kind.

For subsets A and B with same multiplicities the resolution is the same. This resolution can also be expressed as a function of the difference between the two event planes obtained from subsets A and B

$$\begin{aligned}\mathcal{R}_n^A &= \langle\cos\left(n\left(\psi_n^A - \psi_n^{\text{true}}\right)\right)\rangle = \langle\cos\left(n\left(\psi_n^B - \psi_n^{\text{true}}\right)\right)\rangle \\ &= \sqrt{\langle\cos\left(n\left(\psi_n^A - \psi_n^B\right)\right)\rangle}. \end{aligned} \tag{32}$$

Using Eq. (31) the resolution parameter of the subevent, χ_A, can be estimated numerically using the subevent resolution from Eq. (32). The multiplicity of the full event is twice the multiplicity of one subevent. Therefore the resolution parameter of the full event is

$$\chi = \sqrt{2}\chi_A. \tag{33}$$

The event plane resolution of the full event can be then calculated using Eq. (31) with the resolution parameter of the full event from Eq. (33).

3.2 Unfolding procedure

The flow coefficients are not constant event-by-event, because of fluctuations in the initial conditions. In addition to average values the distributions of v_n coefficients are important observables in heavy-ion collisions. Unfortunately the experimental methods have their own uncertainties and they smear the distribution. To get the true distribution one must be able to remove these effects.

The process of removing the smearing from experimental methods is known as unfolding. Unfolding can be used to get the true distribution from the observed distribution. In this thesis I use a data-driven method based on a Bayesian unfolding procedure [106]. The method uses a response function $p\left(v_n^{obs}|v_n\right)$ and an initial guess of the shape of the distribution to construct the response matrix.

First I calculate the v_n coefficients for each event. In this calculation I don't use the event plane method, because it produces also a certain amount of negative values. These are problematic for the unfolding procedure. Instead I calculate the flow vector $\bar{v}_n^{obs} = \left(v_{n,x}^{obs}, v_{n,y}^{obs}\right)$ which is the normalised Q-vector.

$$\begin{aligned} v_{n,x}^{obs} &= \frac{1}{N_{ch}}\sum_{i=1}^{N_{ch}}\cos(n\phi_i) \\ v_{n,y}^{obs} &= \frac{1}{N_{ch}}\sum_{i=1}^{N_{ch}}\sin(n\phi_i) \end{aligned} \tag{34}$$

The magnitude of the flow vector gives the flow coefficient

$$v_n^{obs} = \sqrt{\left(v_{n,x}^{obs}\right)^2 + \left(v_{n,y}^{obs}\right)^2} \tag{35}$$

The next step is determining the response function. I do this with a two-subevent method. I randomly divide charged particles into two subevents and for both subevents I calculate $\bar{v}_n^{obs}$ separately. The smearing is estimated from the distribution of the difference of the flow vectors between the two sub events.

$$p\left(\bar{v}_n^a - \bar{v}_n^b\right) = p\left(v_{n,x}^a - v_{n,x}^b, v_{n,y}^a - v_{n,y}^b\right) \tag{36}$$

For this distribution the physical flow signal is canceled out [106]. The distribution is well described by a 2 dimensional Gaussian with identical widths, δ_{2se}, in both dimensions.

This distribution is related to the $\left(v_n^{obs}, v_n\right)$ distribution.

$$p\left(\bar{v}_n^{obs}|\bar{v}_n\right) = \frac{1}{2}p\left(\bar{v}_n^a - \bar{v}_n^b\right) \approx \frac{1}{2\pi\sigma_n^2} e^{\frac{-\left(\bar{v}_n^{obs} - \bar{v}_n\right)^2}{2\sigma_n^2}}, \tag{37}$$

where $\sigma_n = \sigma_{2se}/2$. The 1-dimensional response function can then be obtained by integrating out the azimuthal angle from the 2-dimensional Gaussian. The result is

$$p\left(v_n^{obs}|v_n\right) \approx \frac{1}{2\pi\sigma_n^2} e^{-\frac{\left(v_n^{obs}\right)^2 + v_n^2}{2\sigma_n^2}} I_0\left(\frac{v_n^{obs} v_n}{\sigma_n^2}\right), \tag{38}$$

where I_0 is the modified Bessel function of the first kind and $\sigma_n = \sigma_{2se}/2$ [106].

After constructing the response function I make an initial guess about the true v_n distribution. As an estimate I use the distribution

$$p\left(v_n\right) = \frac{v_n}{\sigma^2} e^{-\frac{v_n^2}{2\sigma^2}}, \tag{39}$$

As shown in appendix A this is the radial projection of a 2 dimensional Gaussian distribution in $\bar{v}_n$. The σ parameter is given by $\sigma = \sqrt{2/\pi}\left\langle v_n \right\rangle$. Since the event plane method produces a good estimate of the average v_n I use the average $\langle v_n \rangle$ from the event plane method. The function in Eq.39 describes the v_3 distributions well but fails for v_2 beyond the top 2% most central collisions [98]. For the unfolding procedure it is not crucial for the initial guess to have the exact form of the true distribution. The unfolding procedure is able to retrieve the true distribution even with a worse initial guess.

The initial guess gives the probability of having a certain v_n value. The expected number of events with this value is then

$$N\left(v_n\right) = N_{\text{events}} p\left(v_n\right). \tag{40}$$

After this I use the response function from Eq. (38) to calculate the probability of having a certain observed v_n^{obs} value. Then the number of events with certain v_n and v_n^{obs} is

$$N\left(v_n, v_n^{\text{obs}}\right) = N\left(v_n\right) p\left(v_n^{obs} | v_n\right) \tag{41}$$

The calculated numbers of expected $\left(v_n, v_n^{obs}\right)$ pairs make the response matrix, that is used for unfolding. The true v_n distribution is obtained with a Bayesian unfolding procedure from [107]. For the unfolding in ROOT I use the RooUnfold package [108].

In the Bayesian unfolding method the true distribution (cause "c") is obtained with an iterative algorithm starting from the response matrix and from the measured distribution (effect "e").

The first step of the iteration uses the response matrix as the unfolding matrix M^0. This is then used to get the first c^1 from the observed distribution $\hat{e}$.

$$c^{iter+1} = M^{iter} \hat{e}. \tag{42}$$

The c^1 distribution is then used to calculate the second unfolding matrix M^1.

$$M_{i,j}^{iter} = \frac{A_{j,i} c_i^{iter}}{\sum_{m,k} A_{m,i} A_{j,k} c_k^{iter}}, \tag{43}$$

where $A_{j,i} = p\left(e_j | c_i\right)$ is the response function. This process is then iterated. The number of iterations required is relatively small. The v_2 and v_3 distributions I studied converged already after 4-6 iterations.

3.2.1 Monte Carlo test of Unfolding

I tested the unfolding procedure with a simple toy Monte Carlo simulation. In the toy Monte Carlo I generate the v_2 and v_3 coefficients for each event from the distribution

$$p\left(v_n\right) = \frac{v_n}{\sigma^2} e^{-\frac{v_n^2}{2\sigma^2}} \tag{44}$$

where $\sigma = \sqrt{2/\pi}\left\langle v_n \right\rangle$.

The values I used for $\left\langle v_n \right\rangle$ are shown in Tab. 1. In this toy Monte Carlo I used the same value for $\left\langle v_2 \right\rangle$ and $\left\langle v_3 \right\rangle$ for each run. This is to test if there are any differences between the different harmonics that are not related to the magnitude of that harmonic. The values I used for $\left\langle v_2 \right\rangle$ are in the range of LHC measured values

in different centralities as shown in Fig. 18. After generating the v_n coefficients I use the distribution from Eq. (24) to generate azimuthal angles of particles. In this simulation I use constant multiplicity in events.

Parameter	value
$\langle v_2 \rangle$	0.02, 0.03, 0.05, 0.07, 0.10
$\langle v_3 \rangle$	0.02, 0.03, 0.05, 0.07, 0.10
Number of events	1 000 000
Multiplicity per event	500

Table 1: Toy Monte Carlo parameters

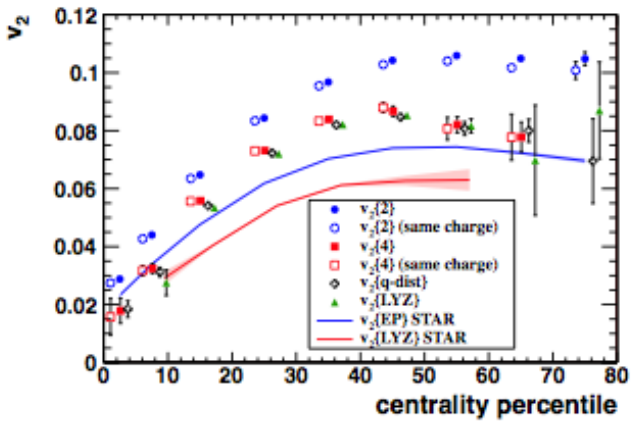

Figure 18: The measured v_2 as a function of multiplicity by ALICE [109].

I calculate the v_n values and their distribution using Eq. (34, 35). In addition to this I calculate the average v_n^{EP} coefficients using the event plane method from Section 3.1 correcting with the event plane resolution. I make an initial guess based on Eq. (44) where I use the average corrected v_n^{EP} as $\langle v_n \rangle$, then generate a response matrix using Eq. 38. Using this response matrix I do the Bayesian unfolding.

Response matrices for two cases are shown in Fig. 19. It can be seen that in the large v_2 case there is a relatively good correlation between observed and true v_2. For the small v_2 case correlation is weak. The unfolding produces relatively good results also in this case, but observing a large v_n value in a single event does not mean that the true anisotropy is strong.

One of the goals of future research is to separate events with small and large v_2 or v_3 coefficients and study jet observables like R_{AA} separately for small and large flow events. In studies like this it is important to know the shape of the response

matrix to be able to estimate how well the measured flow correlates with the true flow.

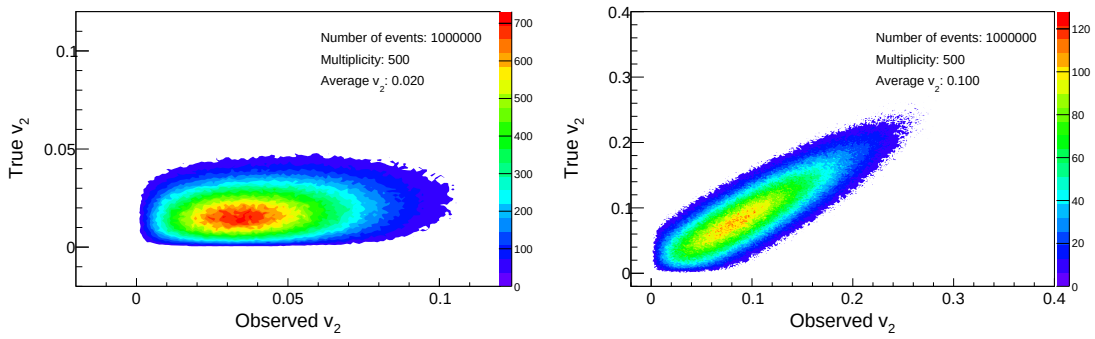

(a) $\langle v_2 \rangle = 0.02$ (b) $\langle v_2 \rangle = 0.10$

Figure 19: Response matrices in toy Monte Carlo. These are filled by the observed v_2 and input v_2 of each event.

The final results from the toy Monte Carlo for unfolding with $\langle v_2 \rangle = \langle v_3 \rangle = 0.03$ are shown in Fig. 20. It can be seen that there is no difference in measuring v_2 and v_3 when the magnitude is the same.

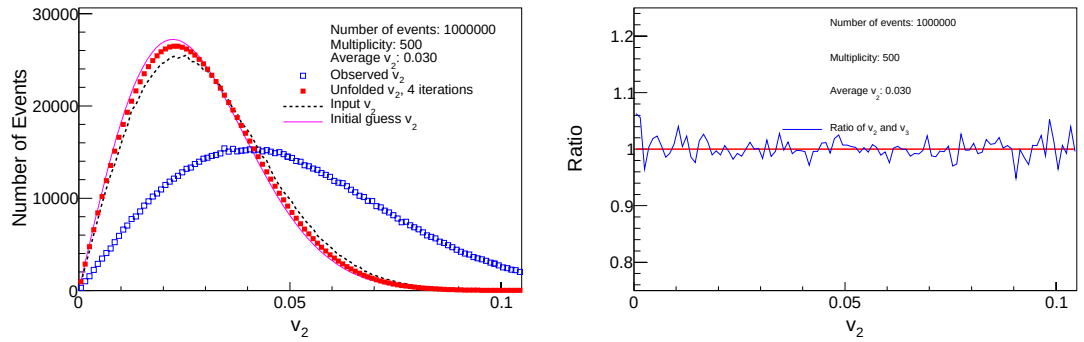

(a) Unfolding in toy Monte Carlo for v_2 (b) Ratio between v_2 and v_3 observed histograms

Figure 20: Toy Monte Carlo results in unfolding for v_2 and v_3.

Results for different magnitudes of flow coefficients are shown in Fig. 21. It can be seen that for larger values of v_2 and v_3 the original distribution is retrieved. However for $\langle v_2 \rangle \leq 0.03$ there is a significant difference between the input and unfolded distributions.

It should be noted that even in this ideal case the observed distribution before unfolding differs significantly from the input distribution. The simulation includes

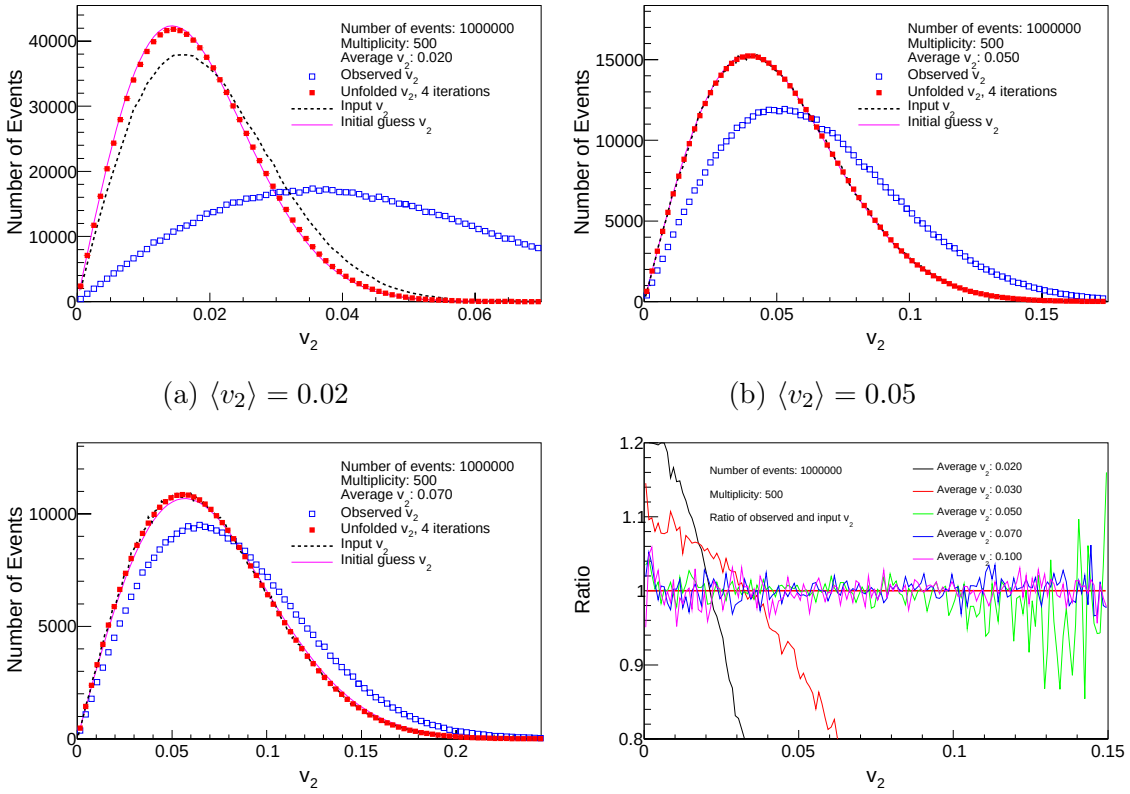

(a) $\langle v_2 \rangle = 0.02$

(b) $\langle v_2 \rangle = 0.05$

(c) $\langle v_2 \rangle = 0.07$

(d) Ratio of unfolded to input

Figure 21: Toy Monte Carlo results for various magnitudes of $\langle v_2 \rangle$

no detector accuracy or efficiency issues. The only reason for not having accurate measurements of v_n is the finite multiplicity. When sampling the $\mathrm{d}N/\,\mathrm{d}\phi$ distribution randomly the result is never a perfect replication of the distribution. One toy Monte Carlo event with multiplicity $N = 400$ is shown in Fig. 22.

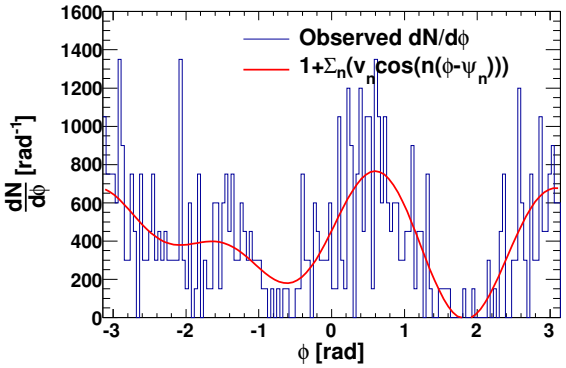

Figure 22: Azimuthal angle distribution from one toy Monte Carlo event with $N = 400$, $v_2 = 0.3$, $v_3 = 0.2$. The observed distribution is overlaid by the input distribution (red line).

4 AMPT model

In this thesis I have studied data simulated using A Multiphase Transport Model (AMPT) [6, 7]. AMPT is a hybrid transport model, which models an ultra-relativistic nuclear collision using many tools of Monte Carlo simulation. There are two versions of AMPT. One is referred to as the default version and the other as AMPT with string melting. The data used in this thesis is generated with the string melting version. The AMPT model consists of four main components. Structure of the string melting version is illustrated in Fig. 23.

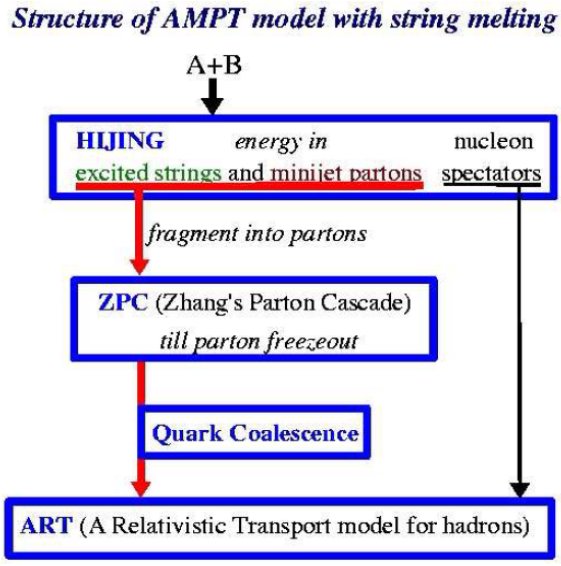

Figure 23: Illustration of the structure of the AMPT model with string melting.

Heavy-ion jet interaction generator (HIJING) model [110] gives the initial conditions, for example spatial and momentum distributions of partons. Scatterings in partonic interactions are handled with Zhang's parton cascade (ZPC) model. Hadronization uses either the Lund string fragmentation model (default AMPT) or a quark coalescence model (AMPT with string melting). The subsequent hadronic matter and its dynamics are then described by a hadronic cascade, based on a relativistic transport (ART) model. The hadronic interactions are terminated at a cutoff time, when the studied observables are considered to be stable. After this cutoff the final results are obtained.

In the HIJING model the two colliding nuclei are assumed to have radial density profiles with Woods-Saxon shapes. Particle production is described in two parts. Hard processes have momentum transfers larger than some cutoff momentum p_0. The current version of AMPT uses 2.0 GeV for the cutoff value. Soft processes have lower momentum transfer values. Hard processes are treated via

the PYTHIA program [76] and evaluated using perturbative QCD (pQCD). The soft part includes non-perturbative processes and is modelled by the formation of strings. In the default model excited strings are assumed to decay independently according to the Lund JETSET fragmentation model [111]. The model with string melting converts excited strings that are not projectile and target nucleons without any interactions to partons according to the flavour and spin structures of their valence quarks. Mesons are converted to quark and antiquark pairs. Baryons and antibaryons are respectively converted to three quarks or three antiquarks, respectively.

The dynamics of the parton phase is solved using the ZPC model. In ZPC two partons undergo scattering whenever they approach each other with a small enough minimal distance. At the moment ZPC includes only parton two-body scatterings such as $gg \to gg$ with cross-sections calculated using pQCD. Minijet partons from hard scatterings can lose energy by gluon splitting and transfer their energies to nearby soft strings in the HIJING model. These mechanisms lead to the so-called jet quenching [6] phenomenon in AMPT. However, the dominant source for jet quenching at high momenta, namely the radiation of energy by the interactions with the medium [112], is not implemented in AMPT.

When partons stop interacting, i.e. they no longer scatter with other partons the hadronization phase starts. In the default AMPT partons are combined with their parent strings to form excited strings. These are then converted to hadrons according to the Lund string fragmentation model. Here it is assumed that strings fragment into quark-antiquark pairs and hadrons are formed from these quarks and antiquarks.

AMPT with string melting uses a simple quark coalescence model, which combines nearby quark-antiquark pairs into mesons and three nearest quarks or antiquarks into baryons or anti-baryons that are close to the invariant mass of these partons. In both AMPT versions the hadrons are given an additional formation time of $0.7\,\mathrm{fm}/c$ during which they are not allowed to scatter with other hadrons during the hadron cascade. Partons freeze out at different times in the parton cascade. Therefore hadronization also occurs at different times and partons coexist with hadrons during the hadronization process.

In AMPT with string melting, strings are melted into soft partons which can undergo only elastic scatterings among themselves and hence the total number of partons in the system is exactly equal to the number of constituent quarks in the produced hadrons.

Hadron cascade in the AMPT model is handled with a relativistic transport model (ART). ART was originally developed to model heavy-ion collisions at AGS energies. ART includes baryon-baryon, baryon-meson and meson-meson elastic and inelastic scatterings.

5 Analysis

5.1 Quark Number Scaling in AMPT Model

5.1.1 Analysis

The AMPT data I use in this thesis is taken from ALICE simulation production [113]. The simulation used the string melting version of AMPT to generate $\sqrt{s_{NN}} = 2.76$ TeV Pb-Pb collision events. The number of events in each centrality bin, and the multiplicity comparison between ALICE and AMPT is shown in Tab. 2. I used the event plane method on the AMPT data to calculate flow coefficients for different particle types. Centralities from 0-5% to 40-50% were studied.

Centrality	0-5%	5-10%	10-20%	20-30%	30-40%	40-50%
ALICE $\mathrm{d}N_{ch}/\mathrm{d}\eta$	1601 ± 60	1294 ± 49	966 ± 37	649 ± 23	426 ± 15	261 ± 9
AMPT $\mathrm{d}N_{ch}/\mathrm{d}\eta$	1514	1231	917	617	403	250
Difference in $\mathrm{d}N_{ch}/\mathrm{d}\eta$	5.7%	5.1%	5.3%	5.2%	5.7%	4.4%
AMPT events	56733	66579	71023	84566	80033	415425
$\mathcal{R}_2$	0.92	0.94	0.96	0.96	0.94	0.91
$\mathcal{R}_3$	0.88	0.87	0.86	0.84	0.83	0.81

Table 2: Comparison of $\mathrm{d}N_{ch}/\mathrm{d}\eta$ for $|\eta| < 0.5$ between data measured at ALICE and data from AMPT simulation. Also the event plane resolutions used to correct v_2 and v_3 are shown.

Charged particles in the pseudorapidity range of $3 < |\eta| < 5$ are used to calculate the event plane angles ψ_2 and ψ_3 using methods explained in section 3.1. The pseudorapidity distribution from AMPT is shown in Fig. 24. The weight used in Eq. (25) is constant 1.

To get the event plane resolution the two sub event method was used as described in Section 3.1.1. In this study the two subsets are taken by dividing the particles randomly to two groups. Obtained resolutions are also shown in Tab. 2.

Calculated event plane angles were then used to calculate flow coefficients of different charged particle species in the mid-rapidity region with $|\eta| < 0.8$. The particles studied here were pions, kaons and protons. Since the range used to calculate event plane angles is outside the mid-rapidity region used to calculate v_n coefficients, there is no need for the removal of auto-correlations.

First the flow coefficients were calculated as a function of the transverse momentum p_{T}. After this the quark number scaling is added as described in section 2.4. Particle masses and quark numbers for studied particles are shown in Tab 3. I also tested the blueshift correction used in Ref. [8] for v_2 of protons. The value

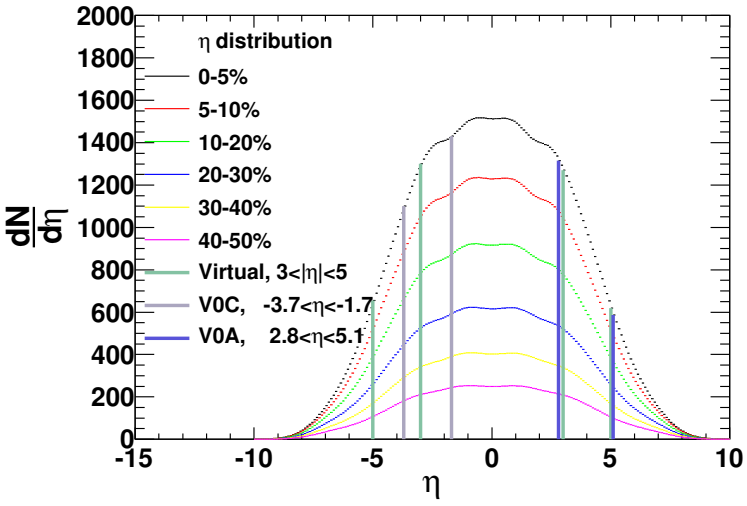

Figure 24: Pseudorapidity distributions in AMPT for different centrality bins. The vertical lines represent pseudorapidity limits of different detectors. V0A and V0C represent detectors at ALICE and the rapidity ranges used in my study are represented by the virtual detector.

I used was a constant 0.15 GeV/c. The correction is applied to the transverse momentum p_{T} before the quark number scaling and calculating KE_T.

Particle type	Pion	Kaon	Proton
Particle mass m [GeV/c]	0.139570	0.493667	0.938272
Number of quarks n_q	2	2	3

Table 3: Particles in AMPT study

5.1.2 Results

In Fig. 25 the calculated flow coefficients v_2 and v_3 are plotted as a function of the transverse momentum p_{T}. The differences between particle species can be seen clearly. Pions and kaons form the meson arm while the protons are the only baryons. The results of quark number scaling are shown in Fig.26. Here is also shown the result of blueshift correction for the proton data. Ratio plots are shown in Fig. 27. The v_n/n_q values of protons and kaons are divided by the corresponding values for pions and plotted as a function of KE_T/n_q. When looking at the ratios there are differences at very low KE_T. In this region v_n coefficients are very

small and thus a small difference between particle species gives a large relativistic difference.

It can be seen that the proton data without corrections are systematically lower than pion and kaon data except for $KE_T \approx 0.4$ GeV/c in peripheral collisions. The quark number scaling as such fails in AMPT as it failed in LHC data. However the scaling is restored in low KE_T with the blueshift correction.

For 0.2 GeV/$c < KE_T < 0.5$ GeV/c the blueshift corrected proton data agrees well with pion and kaon data. At very low KE_T (< 0.2 GeV/c) pion data falls below kaon and corrected proton data. At higher KE_T the proton v_2 is below the pion and kaon v_2 coefficients even with corrections.

For v_3/n_q the values seem to align throughout the KE_T range without any corrections. However the error bars are almost as large as were the differences observed in v_2.

In Fig. 28, 29, 30 v_2, v_2/n_q and ratios to pion v_2/n_q are compared between analysed AMPT data and results from hydrodynamical simulations [60, 61].

From the comparison it can be seen that at low p_{T} and for peripheral collisions AMPT and hydrodynamical models agree. This is the region where flow is believed to be dominated by hydrodynamical expansion. At high p_{T} and in central collisions other effects become prominent.

Also the hydrodynamics calculations seem to break down the quark number scaling. There is no agreement between quark number scaled flow of protons and mesons in neither of the calculations.

5.1.3 Comparison to ALICE Results

Comparisons between particle-specific v_2 coefficients in AMPT and ALICE for pions, kaons and protons are shown in Fig.31. Results from two hydrodynamical simulations by Heinz [60] and Niemi [61] are also shown.

It can be seen that for high p_{T} the AMPT values are significantly below the ALICE measurements. This behaviour was already observed in non-identified flow [105]. For particle identified flow it can be seen that the range in which the AMPT values match the LHC values depends on the particle species. For pions the agreement holds only for $p_{\mathrm{T}} \lesssim 0.6$ GeV/c, but for kaons and protons the ranges of agreement go up to $p_{\mathrm{T}} \approx 1.0$ GeV/c and $p_{\mathrm{T}} \approx 1.5$ GeV/c.

Overlay of quark number scaled values for ALICE, AMPT and hydrodynamical data is shown in Fig. 32. When plotted against the quark number scaled transverse kinetic energy KE_T the ranges of agreement between AMPT and ALICE are about the same for all the particle species.

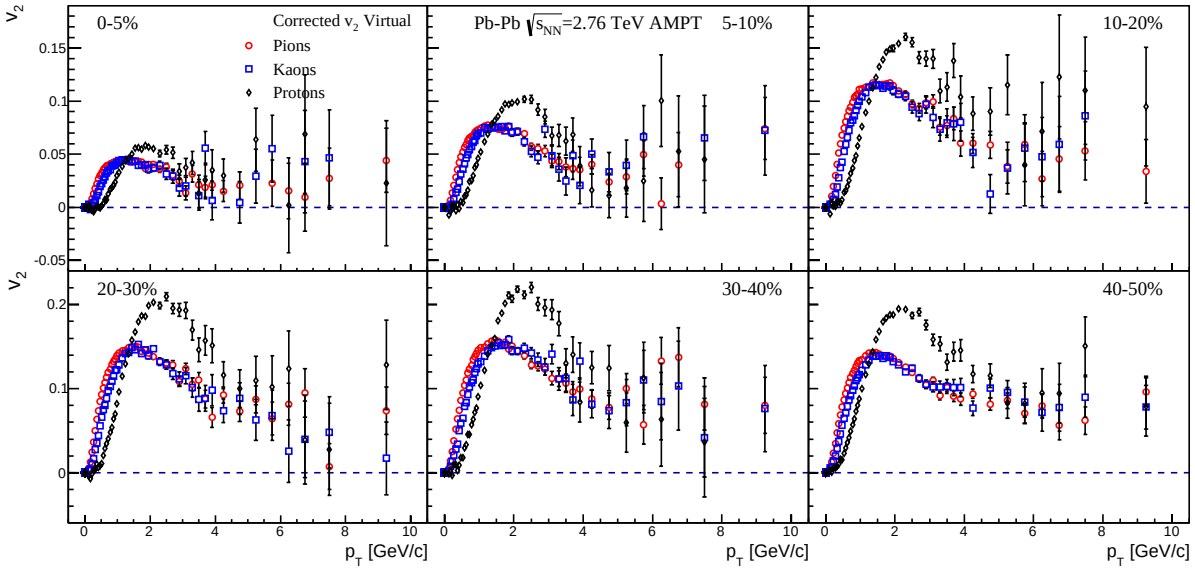

(a) v_2

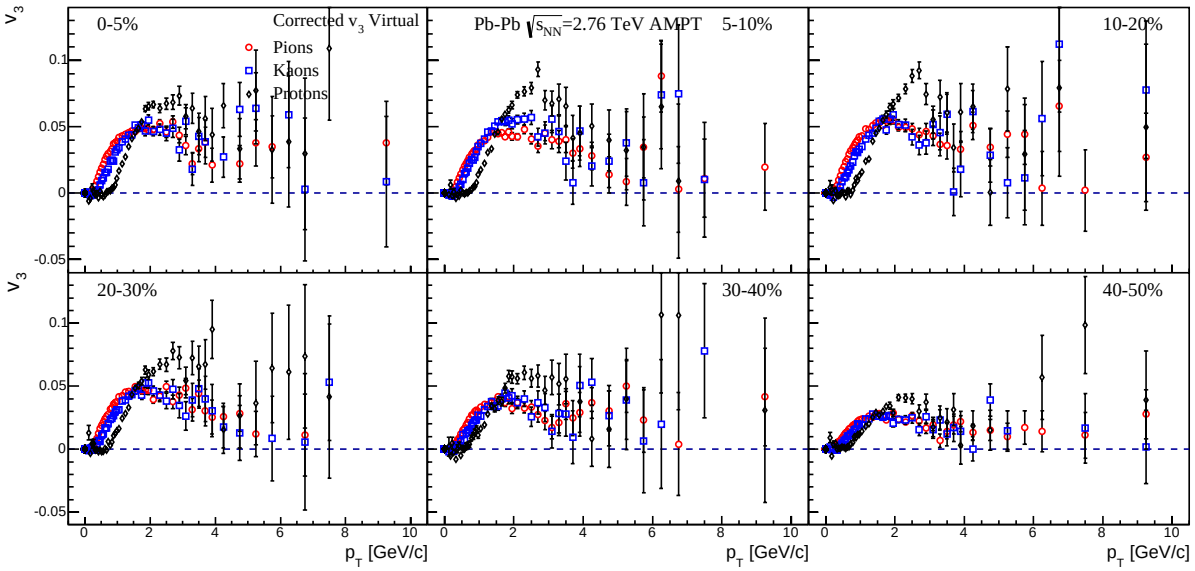

(b) v_3

Figure 25: Particle specific v_2 and v_3 in AMPT.

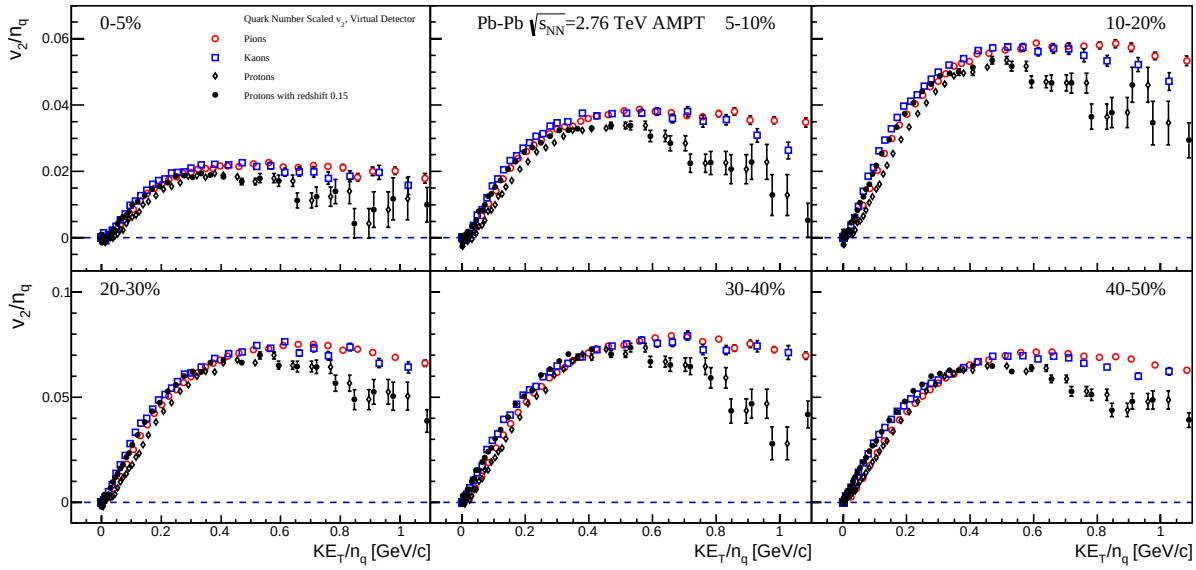

(a) Quark number scaled v_2

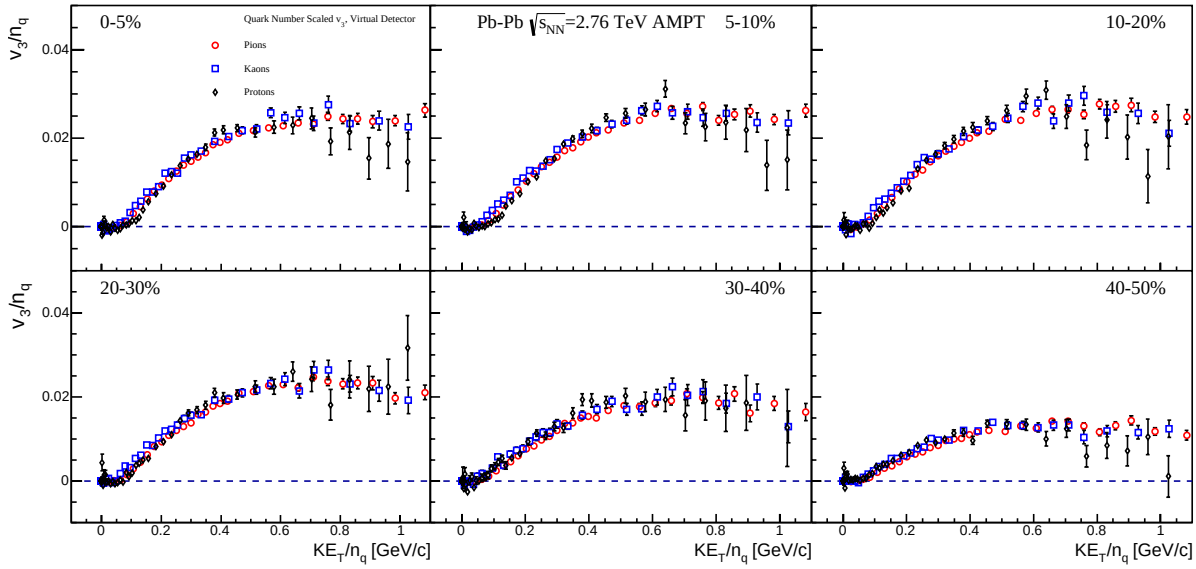

(b) Quark number scaled v_3

Figure 26: Particle specific Quark number scaled v_2 and v_3.

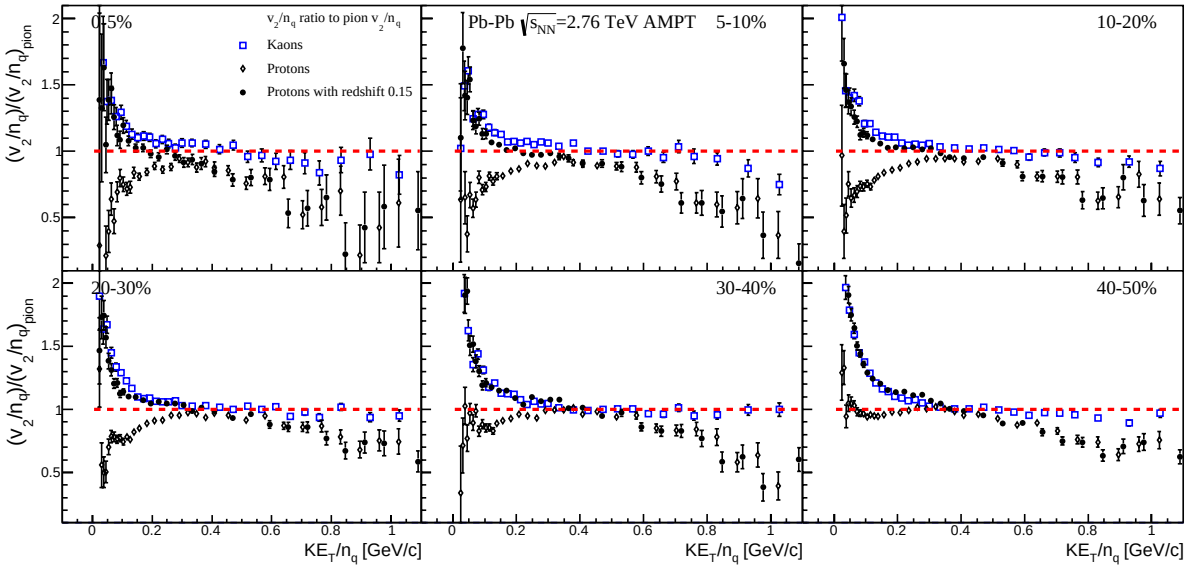

(a) Quark number scaled v_2 ratio to pion v_n/n_q

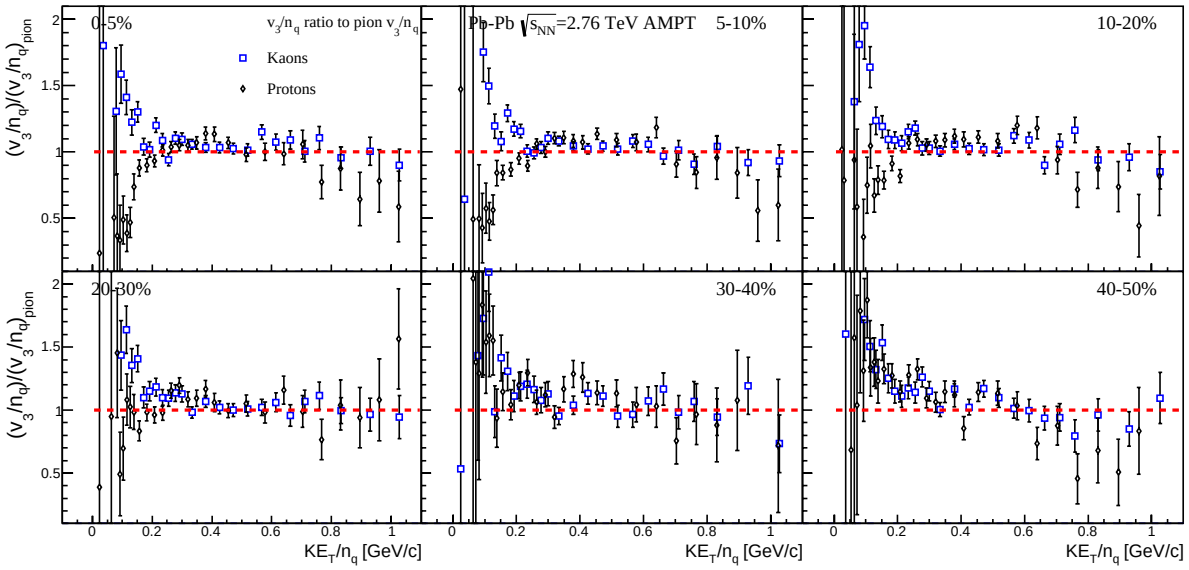

(b) Quark number scaled v_3 ratio to pion v_n/n_q

Figure 27: Comparison of proton and kaon v_n/n_q to pion v_n/n_q plotted as a function of the scaled transverse kinetic energy KE_T/n_q.

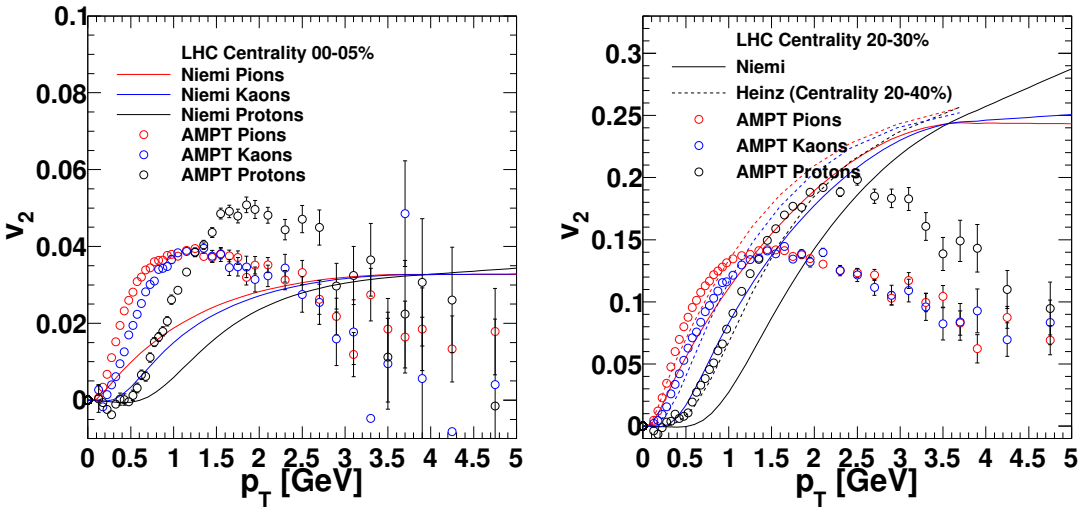

(a) Centrality 0-5% (b) Centrality 20-30%

Figure 28: Comparison of Particle specific v_2 in AMPT and hydrodynamical simulations [60, 61].

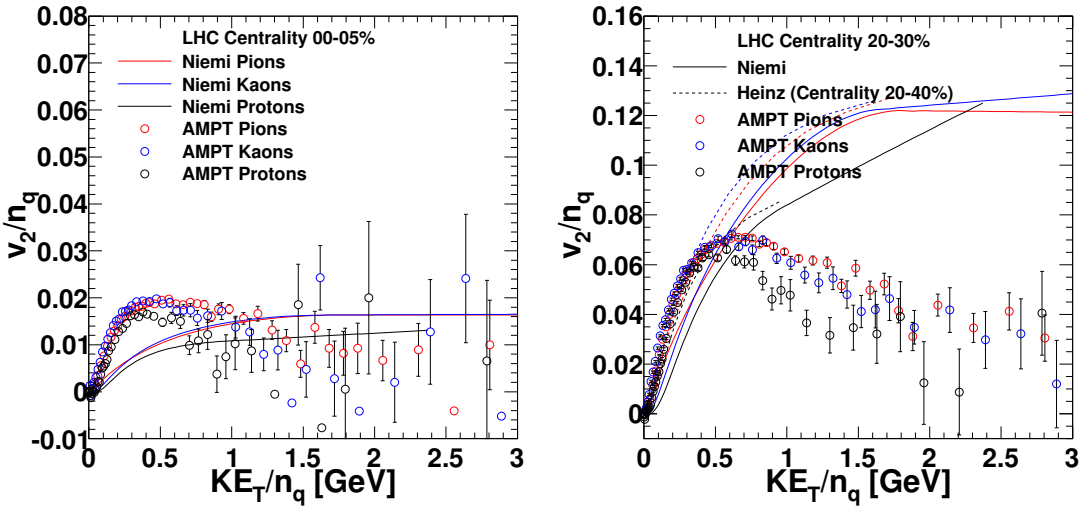

(a) Centrality 0-5% (b) Centrality 20-30%

Figure 29: Comparison of quark number scaled v_2 plotted as a function of the scaled transverse kinetic energy KE_T/n_q in AMPT and hydrodynamical simulations [60, 61].

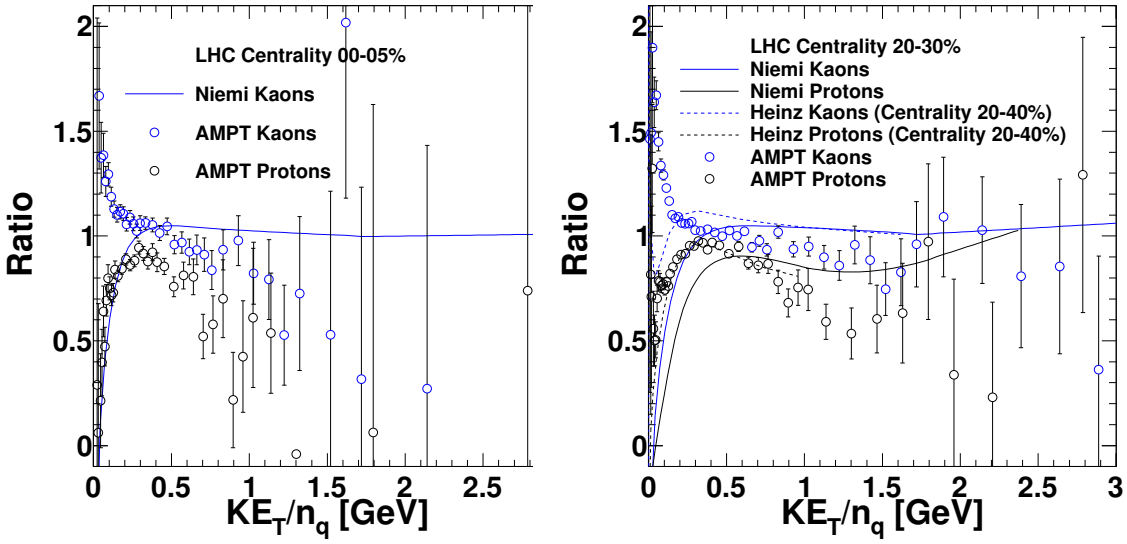

(a) Centrality 0-5%

(b) Centrality 20-30%

Figure 30: Comparison of proton and kaon v_2/n_q to pion v_2/n_q plotted as a function of the scaled transverse energy KE_T/n_q in AMPT and hydrodynamical simulations [60, 61].

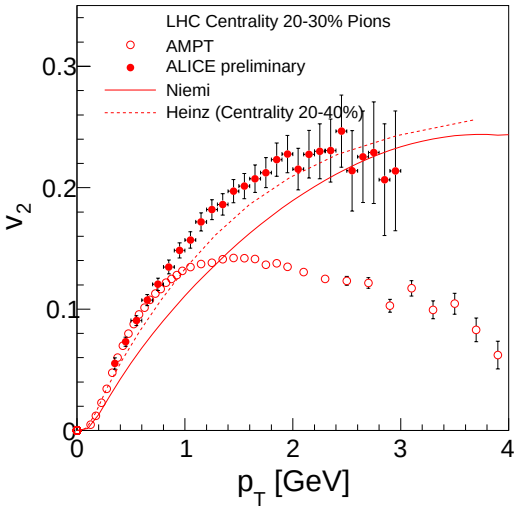

(a) Centrality 20-30%

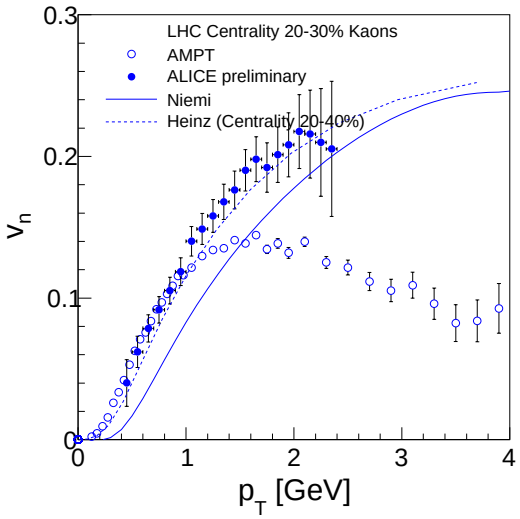

(b) Centrality 20-30%

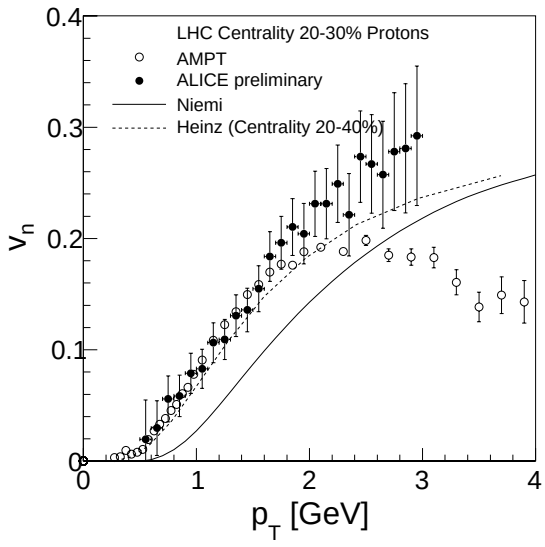

(c) Centrality 20-30%

Figure 31: Comparison of proton, pion and kaon v_2 values in centrality bin 20-30% between AMPT, ALICE and hydrodynamical simulations [60, 61].

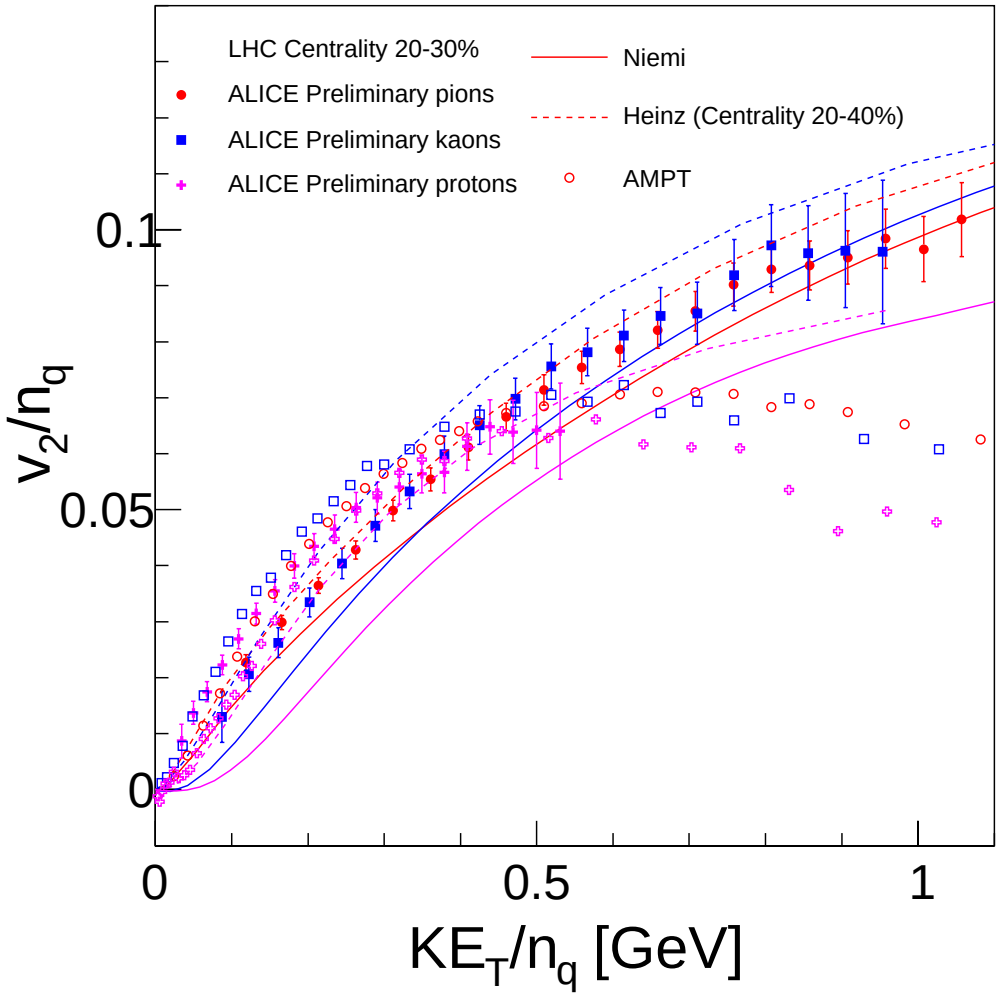

Figure 32: Quark number scaled v_2 for AMPT, ALICE preliminary and hydrodynamical simulations [60, 61].

5.2 Unfolding in AMPT

After identified particle flow I studied event-by-event distributions in AMPT. I calculated $\bar{v}_n^{obs} = \left(v_{n,x}^{obs}, v_{n,y}^{obs}\right)$ for particles in mid-rapidity $|\eta| < 0.8$ and $p_{\mathrm{T}} > 0.1$ GeV/c. I applied the unfolding method given in Sec. 3.2 also to AMPT data. Statistics used for each centrality bin as well as average v_n coefficients are shown in Tab. 4. The unfolding results for v_2 and v_3 are shown in Fig. 33. For v_2 the average value for peripheral collisions is large enough to provide accurate unfolding based on the toy Monte Carlo simulation. Also for the central collisions the multiplicity is high enough even though the average v_2 is in the range with worse unfolding performance. The unfolded v_2 distributions should therefore match the true distribution well.

Centrality	0-5%	5-10%	10-20%	20-30%	30-40%	40-50%
Events	56733	66579	71023	84566	80033	415425
$\langle N_{ch} \rangle$ ($\|\eta\| < 0.8$, $p_{\mathrm{T}} > 0.1$ GeV/c)	2423	1971	1471	990	647	401
Unfolding $\langle v_2 \rangle$	0.028	0.041	0.058	0.072	0.078	0.077
Unfolding $\langle v_3 \rangle$	0.016	0.018	0.018	0.016	0.012	0.0078

Table 4: Number of events used in AMPT study and the average multiplicity used to calculate v_2 and v_3. Also shown are the average values of unfolded v_2 and v_3 distributions.

It can be seen that the v_2 distributions in peripheral collisions do not look like the radial projection of a two dimensional Gaussian shown in Eq. (39). It looks more like a regular Gaussian. This was the distribution used in the toy Monte Carlo and as an initial guess. This is not surprising since this distribution is connected to flow caused purely by fluctuations and v_2 in peripheral collisions is mainly caused by the geometrical asymmetry in the collision.

The average value for v_3 stays at a relatively constant value of 0.16 between the different centrality bins until it drops at centralities larger than 40%. In central collisions the multiplicity is however higher than the one used in the toy Monte Carlo. This might be enough for the method to provide accurate results. In peripheral collisions the multiplicity is even below the values that were tested in the toy Monte Carlo simulation. At these values the unfolding method cannot be expected to give accurate results.

It can be seen that for v_3 in peripheral collisions the unfolded distributions agree with the initial guess. This is expected since in events with low multiplicity and low v_3 values the initial guess dominates the unfolding result.

To get an additional estimate of the performance of unfolding in AMPT I ran the toy Monte Carlo simulation using detected multiplicities and $\langle v_n \rangle$ values. The

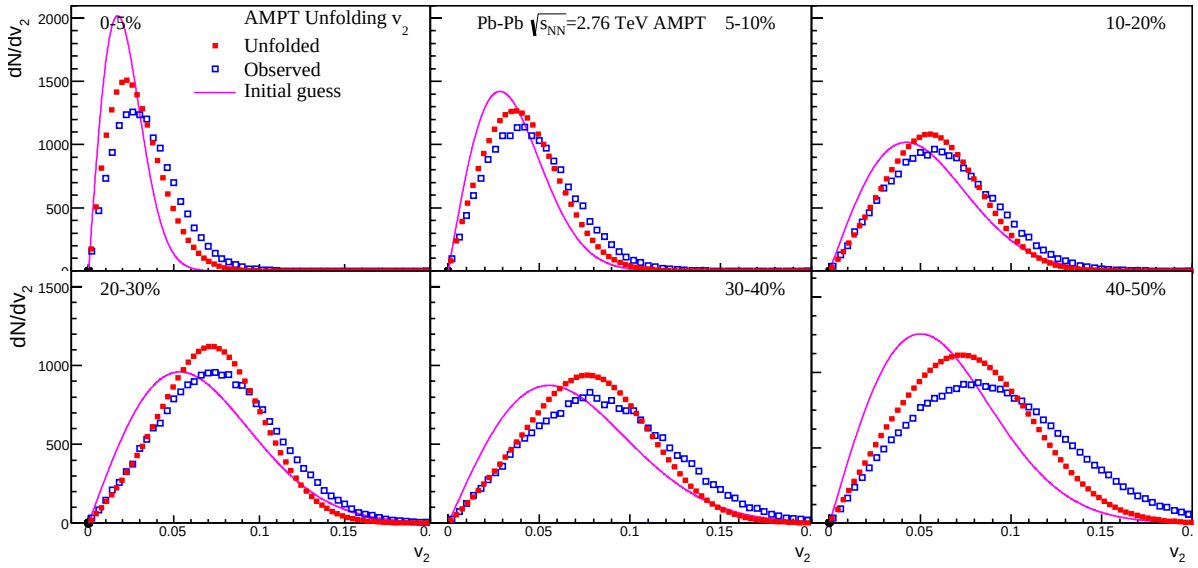

(a) Unfolded v_2 in AMPT

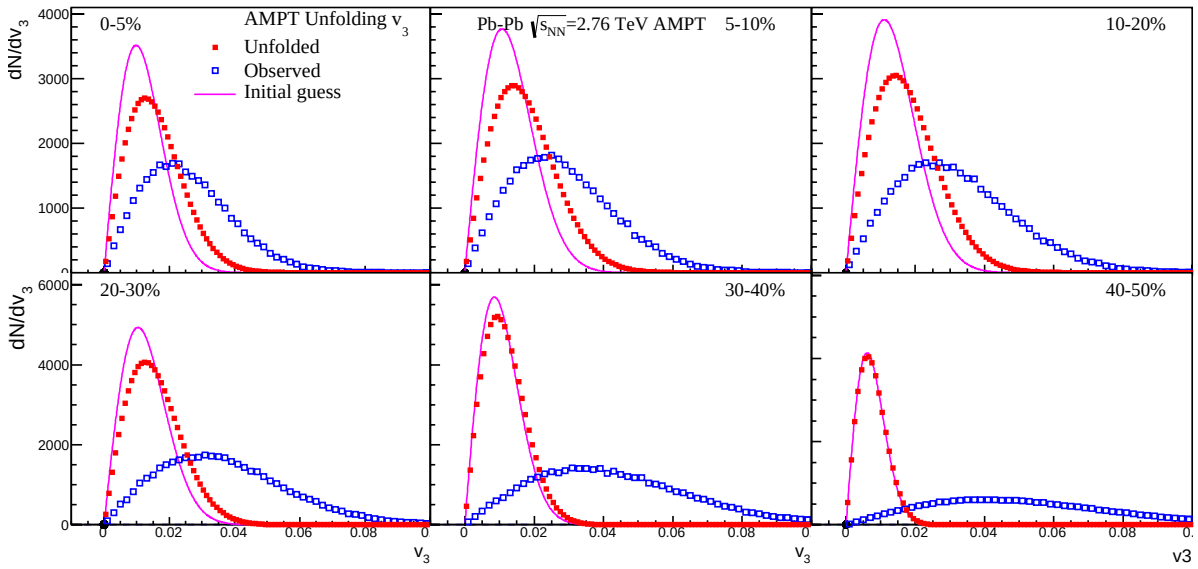

(b) Unfolded v_3 in AMPT

Figure 33: Unfolding results in AMPT

ratios of unfolded and input distributions are shown in Fig. 34. It can be seen that for v_2 the method gives accurate results. For v_3 in centralities up to 20% agreement between input and unfolded distributions is within 10%. For v_3 in more peripheral collisions the method fails to reproduce the input distribution.

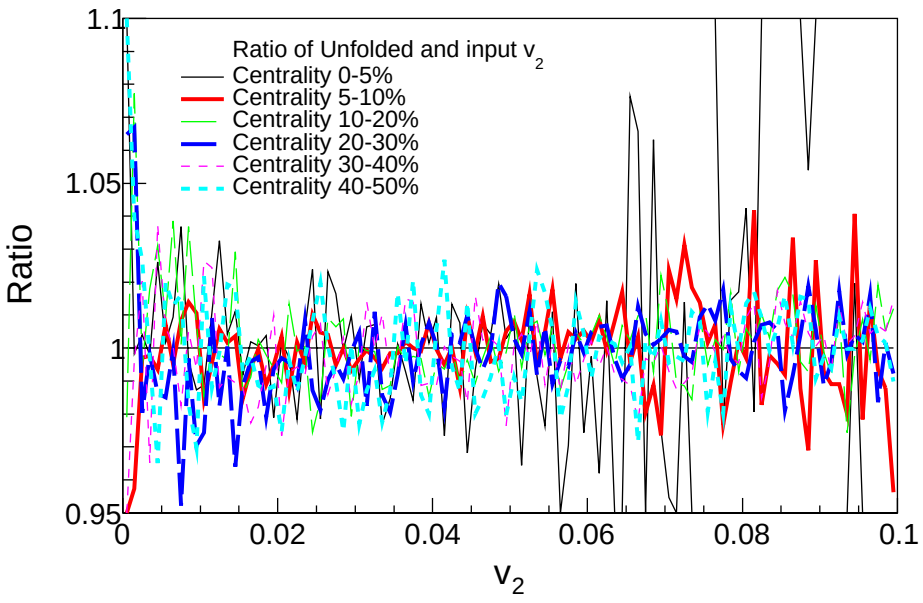

(a) v_2

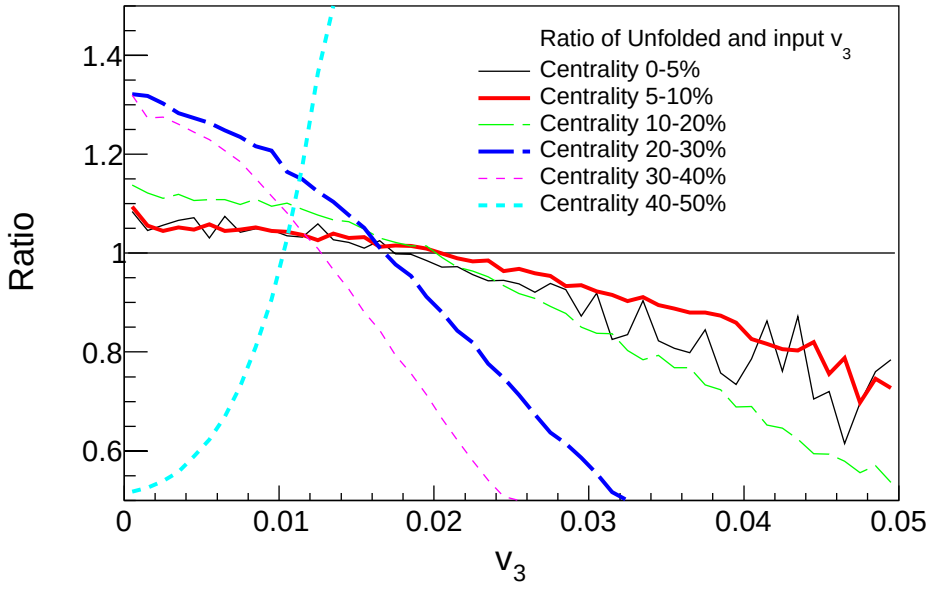

(b) v_2

Figure 34: Unfolding in Toy Monte Carlo with parameters from AMPT. The centrality labels refer to the centrality bin in AMPT from where the parameters N_{ch} and $\langle v_n \rangle$ were taken.

6 Discussion

6.1 Identified Particle Flow and Quark Number Scaling

First of the two main goals of this thesis was studying identified particle flow in AMPT. At RHIC in Au-Au collisions with $\sqrt{s_{NN}} = 200$ GeV it was found out that plotting the quark number scaled transverse kinetic energy versus the quark number scaled v_2 gives an almost perfect scaling between different particle species. This was taken as a strong indication that anisotropic flow at RHIC develops primarily in the partonic phase, and is not strongly influenced by the subsequent hadronic phase [8]. It has already been observed that at LHC energies this scaling does not work. Quark number scaling observed at RHIC was explained by a simple quark coalescence model. Since hadrons are simply combinations of the constituent quarks, flow in the deconfined phase is directly transformed into flow in the hadronic phase. The coalescence model has been challenged after the LHC observations. The AMPT model I study uses this coalescence model, but as I have presented in this thesis, AMPT data has similar scaling properties as the LHC data.

Because of the quark coalescence any differences in flow between different particle species has to develop in the hadronic phase, which seems to affect the flow at LHC energies. AMPT treats the hadronic phase with the ART model. To confirm the effect of the hadronic phase one could turn off the hadron cascade in AMPT and look at flow immediately after hadronization. This has not been done and it might be an interesting topic for future research.

I presented analysis of identified particle flow in the AMPT model for Pb-Pb collisions with $\sqrt{s_{NN}} = 2.76$ GeV. I had previously studied [105] the flow coefficients in AMPT data and now I expanded the study to particle identified flow of pions, kaons and protons in different centrality bins.

I tested the quark number scaling properties of AMPT with v_2 and v_3 and compared the v_2 results to ALICE preliminary data and hydrodynamical calculations. I had previously observed [105] that AMPT reproduces the charged particle v_n values observed at LHC only for $p_{\mathrm{T}} \lesssim 1$ GeV/c and fails at higher p_{T}. The same can be seen in the particle identified data. However the range of agreement between AMPT and LHC data depends on the particle species. For pions the disagreement begins already at $p_{\mathrm{T}} \approx 0.5$ GeV/c, but for kaons and protons the thresholds are 1 GeV/c and 1.5 GeV/c respectively. The dominant source for jet quenching at high momenta, namely the radiation of energy by the interactions with the medium [112], is not implemented in AMPT. Thus it is not surprising that it fails at high p_{T}.

When studying quark number scaling AMPT and LHC data behave similarly. Scaling works well for pions and kaons except for very low KE_T. For protons

scaling breaks down also at higher KE_T. Based on the ALICE data it was observed that redshifting the proton p_{T} with 0.20 GeV/c restores scaling between protons and mesons [8]. In AMPT a proton redshift of similar size restores scaling except for high KE_T.

6.2 Unfolding Event-by-Event Distributions

The second objective was studying event-by-event distributions and unfolding these distributions. I presented results of v_2 and v_3 distributions in AMPT. I applied a Bayesian unfolding method to the distributions to get estimates of the true distributions. I tested the unfolding procedure in a simple Monte Carlo simulation with various multiplicities and magnitudes of flow. For multiplicities and v_2 values corresponding to the AMPT results the method reproduced the true distribution. For v_3 the signal is weaker which makes measuring it more difficult. The simulation gave reasonable results also for v_3 with parameters corresponding to central collisions, where the multiplicity is highest. For more peripheral collisions lower multiplicity limits the accuracy and for centralities larger than 20% the procedure fails to reproduce the input distribution.

It should be noted that even in the ideal Monte Carlo simulation the observed distribution before unfolding differs significantly from the input distribution. The simulation includes no detector accuracy or efficiency issues. The only reason for not having accurate measurements of v_n is the finite multiplicity. When sampling the $\mathrm{d}N/\,\mathrm{d}\phi$ distribution randomly the result is never a perfect replication of the distribution. Weaker signals make the measurement even harder.

In real measurements detector accuracy and nonflow effects further complicate the measurement. The effects of nonflow have been studied at PHENIX [114]. They observed that the effect is negligible for central collisions. Jets are rare and include a small amount of particles compared to the total number of particles in a heavy-ion collision. In peripheral collisions where the multiplicity is smaller and flow signal is weaker nonflow is more significant. Nonflow effects include mainly jet effects. Even though the parton that created the jet is very energetic, the fragmentation process produces a number of particles also with small p_{T}. These particles have not been affected by the pressure-driven expansion which caused the flow, so they bring an additional component to the angle distribution. This component makes it harder to detect the actual flow signal.

Based on the Monte Carlo study the unfolded v_2 distributions in AMPT should match the true distributions. Also v_3 distributions in centrality bins 0-20% provided results that were within 10% of the input distribution. For more peripheral collisions with v_3 the unfolding procedure can not be trusted.

7 Summary

In this master's thesis I have studied quark number scaling of identified charged particle flow coefficients and unfolding the distributions of v_2 and v_3 of charged particles in the AMPT model.

I had previously studied [105] the flow coefficients in AMPT data and now I expanded the study to particle identified flow of pions, kaons and protons in different centrality bins. At RHIC it was found out that plotting the quark number scaled transverse kinetic energy versus the quark number scaled v_2 gives an almost perfect scaling. It has already been observed that quark number scaling breaks down at LHC energies. Quark number scaling at RHIC was explained with a quark coalescence model which is implemented in the AMPT model.

I tested the quark number scaling properties of AMPT with v_2 and v_3 and compared the v_2 results to ALICE preliminary data and hydrodynamical calculations. This revealed that the proton v_2 does not match the pion and kaon v_2 values. The difference between proton and meson data is of similar size as measured in ALICE. Correcting proton p_{T} with a redshift of $0.15 - 0.20$ GeV/c returns the scaling between particle species. In AMPT data the redshift correction works for low KE_T, but at high KE_T there is still considerable difference with proton and meson v_2 values.

Previously I had already observed [105] that AMPT reproduces the charged particle v_n values observed at LHC only for $p_{\mathrm{T}} \lesssim 1$ GeV/c and fails at higher p_{T}. The same can be seen in the identified particle data. However, the range of agreement between AMPT and LHC data depends on the particle species. For pions the disagreement begins already at $p_{\mathrm{T}} \approx 0.5$ GeV/c, but for kaons and protons the AMPT data agrees with measured data until 1 GeV/c and 1.5 GeV/c respectively.

Another aspect I studied in this thesis was the unfolding of v_n distributions. I used a data-driven unfolding method, that I first tested with a toy Monte Carlo simulation with different multiplicities and average v_n values. It was found out that the method reproduces the input distribution very well for multiplicities and $\langle v_2 \rangle$ values corresponding to centralities 0-60% and $\langle v_3 \rangle$ values corresponding to centralities 0-20%, but for parameters corresponding to v_3 in more peripheral collisions the method failed to reproduce the input distributions.

Based on this study, unfolded event-by-event distributions of v_2 can be trusted up to centralities 50% and distributions of v_3 can be trusted in centralities 0-20%.

Appendices

A Integration of 2 Dimensional Gaussian Distribution

A Gaussian distribution that is centered at 0 has the form

$$\frac{1}{N}\frac{\mathrm{d}N}{\mathrm{d}x} = \frac{1}{\sigma\sqrt{2\pi}}e^{-\frac{x^2}{2\sigma^2}}$$

The expectation value $\langle x\rangle$ is zero because the distribution is symmetric.

$$\langle x\rangle = 0 \tag{45}$$

The expectation values of $\langle|x|\rangle$ and $\langle x^2\rangle$ are nonzero

$$\begin{aligned}\langle|x|\rangle &= \int_{-\infty}^{\infty}\frac{|x|}{\sigma\sqrt{2\pi}}e^{-\frac{x^2}{2\sigma^2}} = \int_{0}^{\infty}\frac{x}{\sigma\sqrt{2\pi}}e^{-\frac{x^2}{2\sigma^2}} - \int_{-\infty}^{0}\frac{x}{\sigma\sqrt{2\pi}}e^{-\frac{x^2}{2\sigma^2}} \\ &= \frac{\sigma}{\sqrt{2\pi}} + \frac{\sigma}{\sqrt{2\pi}} = \frac{\sqrt{2}\sigma}{\sqrt{\pi}} = \sqrt{\frac{2\sigma^2}{\pi}}. \qquad (46)\\ \left\langle x^2\right\rangle &= \int_{-\infty}^{\infty}\frac{x^2}{\sigma\sqrt{2\pi}}e^{-\frac{x^2}{2\sigma^2}} \qquad (47)\end{aligned}$$

can be done with the following trick

$$\int_{-\infty}^{\infty} e^{-ax^2} = \sqrt{\frac{\pi}{a}}$$

Differentiating with respect to a gives

$$\int_{-\infty}^{\infty} x^2 e^{-ax^2} = \frac{1}{2}\sqrt{\frac{\pi}{a^3}}$$

Inserting $a = 1/2\sigma^2$ gives

$$\int_{-\infty}^{\infty} x^2 e^{-\frac{x^2}{2\sigma^2}} = \sqrt{2\pi}\sigma^3$$

and thus

$$\left\langle x^2\right\rangle = \int_{-\infty}^{\infty}\frac{x^2}{\sigma\sqrt{2\pi}}e^{-\frac{x^2}{2\sigma^2}} = \frac{1}{\sigma\sqrt{2\pi}}\sqrt{2\pi}\sigma^3 = \sigma^2$$

A two dimensional Gaussian distribution has the form

$$\frac{1}{N}\frac{\mathrm{d}N}{\mathrm{d}x\,\mathrm{d}y} = \frac{1}{\sigma_x\sqrt{2\pi}}\frac{1}{\sigma_y\sqrt{2\pi}}e^{-\frac{(x)^2}{2\sigma_x^2}-\frac{y^2}{2\sigma_y^2}} \tag{48}$$

For a symmetric case $\sigma_x = \sigma_y$ this reduces to

$$\frac{1}{N}\frac{\mathrm{d}N}{\mathrm{d}x\,\mathrm{d}y} = \frac{1}{\sigma^2 2\pi}e^{-\frac{(x+y)^2}{2\sigma^2}} \tag{49}$$

A change into polar co-ordinates $\mathrm{d}x\,\mathrm{d}y = r\,\mathrm{d}r\,\mathrm{d}\phi = 2\pi r\,\mathrm{d}r$, gives

$$\frac{1}{N}\frac{\mathrm{d}N}{\mathrm{d}x\,\mathrm{d}y} = \frac{1}{N}\frac{1}{2\pi r}\frac{\mathrm{d}N}{\mathrm{d}r} = \frac{1}{2\pi\sigma^2}e^{-\frac{r^2}{2\sigma^2}}$$

Therefore

$$\frac{1}{N}\frac{\mathrm{d}N}{\mathrm{d}r} = \frac{r}{\sigma^2}e^{-\frac{r^2}{2\sigma^2}} \tag{50}$$

$$\langle|r|\rangle = \langle r\rangle = \int_0^\infty \mathrm{d}r\frac{r^2}{\sigma^2}e^{-\frac{x^2}{2\sigma^2}} = \frac{1}{\sigma^2}\sqrt{2\pi}\sigma^3\frac{1}{2} = \sigma\sqrt{\frac{\pi}{2}} \tag{51}$$

$$\sigma = \sqrt{\frac{2}{\pi}}\,\langle r\rangle \tag{52}$$

References

[1] PHENIX Collaboration, K. Adcox *et al.*, Nucl.Phys. **A757**, 184 (2005), nucl-ex/0410003.

[2] STAR Collaboration, J. Adams *et al.*, Nucl.Phys. **A757**, 102 (2005), nucl-ex/0501009.

[3] J.-Y. Ollitrault, Phys. Rev. D **46**, 229 (1992).

[4] U. Heinz and P. Kolb, Nucl. Phys. **A702**, 269 (2002).

[5] E. Shuryak, Prog. Part. Nucl. Phys. **62**, 48 (2009).

[6] Z.-W. Lin, C. M. Ko, B.-A. Li, B. Zhang, and S. Pal, Phys.Rev. **C72**, 064901 (2005), nucl-th/0411110.

[7] J. Xu and C. M. Ko, Phys.Rev. **C83**, 034904 (2011), 1101.2231.

[8] R. A. Lacey *et al.*, (2012), 1207.1886.

[9] C. M. G. Lattes, G. Occhialini, and C. F. Powell, Nature **160**, 453 (1947).

[10] R. Bjorklund, W. Crandall, B. J. Moyer, and H. York, Phys. Review **77**, 213 (1950).

[11] W. Heisenberg, Zeitschrift für Physik **77**, 1 (1932).

[12] M. Gell-Mann, Phys. Rev. **125**, 1067 (1962).

[13] M. Gell-Mann, Phys. Lett. **8**, 214 (1964).

[14] O. Greenberg, Phys. Rev. Lett. **13**, 598 (1964).

[15] Crystal Ball Collaboration, D. Williams *et al.*, Phys.Rev. **D38**, 1365 (1988).

[16] W. Krolikowski, Nuovo Cim. **A27**, 194 (1975).

[17] D. J. Gross and F. Wilczek, Physical Review Letters **30**, 1343 (1973).

[18] H. D. Politzer, Physical Review Letters **30**, 1346 (1973).

[19] D. J. Gross and F. Wilczek, Physical Review D **8**, 3633 (1973).

[20] D. J. Gross and F. Wilczek, Physical Review D **9**, 980 (1974).

[21] H. Georgi and H. D. Politzer, Physical Review D **9**, 416 (1974).

[22] H. Fritzsch, M. Gell-Mann, and H. Leutwyler, Physics Letters B **47**, 365 (1973).

[23] I. Flegel and P. Söding, CERN courier (2004).

[24] R. Brandelik *et al.*, Physics Letters B **86**, 243 (1979).

[25] J. K. L. MacDonald, Phys. Rev. **43**, 830 (1933).

[26] C. Berger *et al.*, Physics Letters B **86**, 418 (1979).

[27] R. Alkofer and J. Greensite, J.Phys. **G34**, S3 (2007), hep-ph/0610365.

[28] J. Collins and M. Perry, Phys. rev. Lett. **34**, 1353 (1975).

[29] E. Shuryak, Phys. Reps. **61**, 71 (1980).

[30] J. C. Collins, D. E. Soper, and G. F. Sterman, Adv.Ser.Direct.High Energy Phys. **5**, 1 (1988), hep-ph/0409313.

[31] R. Gupta, p. 83 (1997), hep-lat/9807028.

[32] F. Karsch, Lect.Notes Phys. **583**, 209 (2002), hep-lat/0106019.

[33] K. Rajagopal, SLAC Beam Line **31-2**, 9 (2001).

[34] E. Lofgren, *ACCELERATOR DIVISION ANNUAL REPORTS, 1 JULY 1972 12/31/1974* (, 1975).

[35] A. Kovalenko *et al.*, Status of the nuclotron, in *Proceedings of EPAC* Vol. 94, pp. 161–164, 1994.

[36] I. Vitev and M. Gyulassy, Phys.Rev.Lett. **89**, 252301 (2002), hep-ph/0209161.

[37] D. S. Barton, Heavy ion program at bnl: Ags, rhic, in *Proc. 1987 Parti- cle Accelerator Conference, Washington, D.C., March, 1987*, 1987.

[38] NA61/SHINE, K. Grebieszkow, PoS **CPOD2013**, 004 (2013).

[39] BRAHMS Collaboration, I. Arsene *et al.*, Nucl.Phys. **A757**, 1 (2005), nucl-ex/0410020.

[40] B. Back *et al.*, Nucl.Phys. **A757**, 28 (2005), nucl-ex/0410022.

[41] J. D. Bjorken, Phys. Rev. D **27**, 140 (1983).

[42] G. Baym, B. L. Friman, J.-P. Blaizot, M. Soyeur, and W. Czyż, Nuclear Physics A **407**, 541 (1983).

[43] H. von Gersdorff, L. McLerran, M. Kataja, and P. V. Ruuskanen, Phys. Rev. D **34**, 794 (1986).

[44] K. Peeters and M. Zamaklar, Eur.Phys.J.ST **152**, 113 (2007), 0708.1502.

[45] P. Danielewicz and M. Gyulassy, Phys. Rev. D **31**, 53 (1985).

[46] P. Kovtun, D. Son, and A. Starinets, Phys.Rev.Lett. **94**, 111601 (2005), hep-th/0405231.

[47] R. A. Lacey *et al.*, Phys. Rev. Lett. **98**, 092301 (2007).

[48] S. A. Voloshin, A. M. Poskanzer, and R. Snellings, (2008), 0809.2949.

[49] S. A. Voloshin, A. M. Poskanzer, A. Tang, and G. Wang, Phys.Lett. **B659**, 537 (2008), 0708.0800.

[50] H. Holopainen, H. Niemi, and K. J. Eskola, Phys.Rev. **C83**, 034901 (2011), 1007.0368.

[51] ALICE Collaboration, Phys. Rev. C **88**, 044909 (2013).

[52] M. L. Miller, K. Reygers, S. J. Sanders, and P. Steinberg, Ann.Rev.Nucl.Part.Sci. **57**, 205 (2007), nucl-ex/0701025.

[53] R. Glauber, Lectures in theoretical physics, 1959.

[54] W. Czyż and L. Maximon, Annals of Physics **52**, 59 (1969).

[55] A. Białłas, M. Bleszyński, and W. Czyż, Nuclear Physics B **111**, 461 (1976).

[56] PHENIX Collaboration, S. Afanasiev *et al.*, Phys.Rev. **C80**, 054907 (2009), 0903.4886.

[57] J.-Y. Ollitrault, Eur.J.Phys. **29**, 275 (2008), 0708.2433.

[58] P. Romatschke, Int.J.Mod.Phys. **E19**, 1 (2010), 0902.3663.

[59] L. LD, Izv. Akad. Nauk Ser. Fiz. **17**, 51 (1953).

[60] H. Song, S. Bass, and U. W. Heinz, (2013), 1311.0157.

[61] H. Niemi, G. Denicol, P. Huovinen, E. Molnar, and D. Rischke, Phys.Rev. **C86**, 014909 (2012), 1203.2452.

[62] K. A. *et al.* [ALICE Collaboration], Phys. Rev. Lett **106** (2011), 032301.

[63] J.-Y. Ollitrault, Phys.Rev. D **48**, 1132 (1993), hep-ph/9303247.

[64] P. Danielewicz and G. Odyniec, Physics Letters B **157**, 146 (1985).

[65] P. Danielewicz and M. Gyulassy, Physics Letters B **129**, 283 (1983).

[66] T. Abbott *et al.*, Phys. Rev. Lett. **70**, 1393 (1993).

[67] S. Voloshin and Y. Zhang, Z.Phys. **C70**, 665 (1996), hep-ph/9407282.

[68] E877 Collaboration, J. Barrette *et al.*, Phys.Rev.Lett. **73**, 2532 (1994), hep-ex/9405003.

[69] CMS Collaboration, S. Chatrchyan *et al.*, Phys.Rev.Lett. **109**, 022301 (2012), 1204.1850.

[70] A. Majumder and M. Van Leeuwen, Prog.Part.Nucl.Phys. **A66**, 41 (2011), 1002.2206.

[71] F. Dominguez, C. Marquet, A. Mueller, B. Wu, and B.-W. Xiao, Nucl.Phys. **A811**, 197 (2008), 0803.3234.

[72] M. Gyulassy, P. Levai, and I. Vitev, Nucl.Phys. **B571**, 197 (2000), hep-ph/9907461.

[73] U. A. Wiedemann, Nucl.Phys. **B588**, 303 (2000), hep-ph/0005129.

[74] P. B. Arnold, G. D. Moore, and L. G. Yaffe, JHEP **0112**, 009 (2001), hep-ph/0111107.

[75] X.-N. Wang and X.-f. Guo, Nucl.Phys. **A696**, 788 (2001), hep-ph/0102230.

[76] T. Sjostrand, S. Mrenna, and P. Z. Skands, Comput.Phys.Commun. **178**, 852 (2008), 0710.3820.

[77] I. Lokhtin and A. Snigirev, Eur.Phys.J. **C45**, 211 (2006), hep-ph/0506189.

[78] N. Armesto, L. Cunqueiro, and C. A. Salgado, Nucl.Phys. **A830**, 271C (2009), 0907.4706.

[79] K. Zapp, G. Ingelman, J. Rathsman, J. Stachel, and U. A. Wiedemann, Eur.Phys.J. **C60**, 617 (2009), 0804.3568.

[80] T. Renk, Phys.Rev. **C79**, 054906 (2009), 0901.2818.

[81] ALICE Collaboration, K. Aamodt *et al.*, Phys.Lett. **B696**, 30 (2011), 1012.1004.

[82] WA98 Collaboration, M. Aggarwal *et al.*, Eur.Phys.J. **C23**, 225 (2002), nucl-ex/0108006.

[83] D. G. d'Enterria, Phys.Lett. **B596**, 32 (2004), nucl-ex/0403055.

[84] PHENIX Collaboration, A. Adare *et al.*, Phys.Rev.Lett. **101**, 232301 (2008), 0801.4020.

[85] STAR Collaboration, J. Adams *et al.*, Phys.Rev.Lett. **91**, 172302 (2003), nucl-ex/0305015.

[86] A. Dainese, C. Loizides, and G. Paic, Eur.Phys.J. **C38**, 461 (2005), hep-ph/0406201.

[87] I. Vitev, J.Phys. **G30**, S791 (2004), hep-ph/0403089.

[88] C. A. Salgado and U. A. Wiedemann, Phys.Rev. **D68**, 014008 (2003), hep-ph/0302184.

[89] N. Armesto, A. Dainese, C. A. Salgado, and U. A. Wiedemann, Phys.Rev. **D71**, 054027 (2005), hep-ph/0501225.

[90] T. Renk, H. Holopainen, R. Paatelainen, and K. J. Eskola, Phys.Rev. **C84**, 014906 (2011), 1103.5308.

[91] CMS Collaboration, S. Chatrchyan *et al.*, Eur.Phys.J. **C72**, 1945 (2012), 1202.2554.

[92] PHENIX Collaboration, S. Afanasiev *et al.*, Phys. Rev. C **80**, 054907 (2009).

[93] ALICE Collaboration, K. Aamodt *et al.*, Phys.Rev.Lett. **108**, 092301 (2012), 1110.0121.

[94] A. P. Mishra, R. K. Mohapatra, P. Saumia, and A. M. Srivastava, Phys.Rev. **C77**, 064902 (2008), 0711.1323.

[95] A. Mocsy and P. Sorensen, (2010), 1008.3381.

[96] B. Alver and G. Roland, Phys.Rev. **C81**, 054905 (2010), 1003.0194.

[97] J. Xu and C. M. Ko, Phys.Rev. **C84**, 014903 (2011), 1103.5187.

[98] ATLAS Collaboration, J. Jia, Nucl.Phys.A904-905 **2013**, 421c (2013), 1209.4232.

[99] K. A. *et al.* [ALICE Collaboration], Phys. Rev. Lett. **107** (2011), 032301.

[100] K. Aamodt *et al.*, Physics Letters B **708**, 249 (2012).

[101] B. Schenke, S. Jeon, and C. Gale, Phys.Lett. **B702**, 59 (2011), 1102.0575.

[102] ALICE Collaboration, B. Abelev *et al.*, Phys.Rev. **C88**, 044910 (2013), 1303.0737.

[103] A. A. *et al.* [PHENIX Collaboration], PRL **98** (2008), 162301.

[104] D. Molnar and S. A. Voloshin, Phys.Rev.Lett. **91**, 092301 (2003), nucl-th/0302014.

[105] T. Snellman, Event plane determination and fluctuating events in heavy-ion collisions, Bachelor's thesis, University of Jyväskylä, Finland, 2012.

[106] J. Jia and S. Mohapatra, Phys.Rev. **C88**, 014907 (2013), 1304.1471.

[107] G. D'Agostini, Nucl. Instrum. Meth. A **362**, 487 (1995).

[108] Roounfold: Root unfolding framework, `http://hepunx.rl.ac.uk/~adye/software/unfold/RooUnfold.html`, 2013.

[109] ALICE Collaboration, K. Aamodt *et al.*, Phys.Rev.Lett. **105**, 252302 (2010), 1011.3914.

[110] X.-N. Wang and M. Gyulassy, Phys. Rev. **D 44** (1991), 3501Ð3516.

[111] T. Sjostrand, Comput.Phys.Commun. **82**, 74 (1994).

[112] D. d'Enterria, (2009), 0902.2011.

[113] Alice repository, `http://alimonitor.cern.ch/job_details.jsp`, 2012.

[114] PHENIX Collaboration, A. Adare *et al.*, Phys.Rev. **C78**, 014901 (2008), 0801.4545.